AN ALL-SKY SEARCH FOR CONTINUOUS GRAVITATIONAL WAVES

by

Vladimir Dergachev

A dissertation submitted in partial fulfillment
of the requirements for the degree of
Doctor of Philosophy
(Physics)
in The University of Michigan
2009

Doctoral Committee:

Professor Keith Riles, Chair
Professor Dante Eric Amidei
Professor Timothy A. McKay
Assistant Professor Dragan Huterer
Assistant Professor Stilian Atanasov Stoev

ACKNOWLEDGEMENTS

In books one can read about an age of science, when pursuit of knowledge was considered to be a worthy cause in itself and when rational thought and understanding of physical world were deemed a necessity. One hears about the excitement of a search and joy of discovery, and of fellow scientists with whom to admire a beautiful equation or an ingenious apparatus. Was this ever so and have some islands survived to this day ?

I would like to thank Keith Riles for making it possible for me to touch a dream and make part of it real, for his delightful popcorn meetings and late evening e-mails when we had new results.

This work would not have been possible without the efforts of many people that made LIGO a success. I would especially like to thank reviewers of PowerFlux - Peter Shawhan, Teviet Creighton, Fred Raab, B. Sathyaprakash and Phil Willems - for putting up with a line-by-line walkthrough of tens of thousands of lines of code.

I have enjoyed many wonderful courses in the University of Michigan Physics department - too bad there are many that I had to miss.

My big thanks and encouragement go to my wife Anna Amirdjanova and my daughter Katie.

The design of the wavefront camera was made easier by integrated circuit samples kindly provided by Analog Devices, JDS Uniphase, National Semiconductor and Optek.

TABLE OF CONTENTS

LIST OF FIGURES

Figure

LIST OF TABLES

Table

CHAPTER I

Introduction

One of the most remarkable facts about physical world is the almost perfect uniformity that meshes so well with convenient mathematical tools. In part, this is due to the enormous numbers of elementary particles, but this is not the whole story. Consider, for example, that 1 cubic centimeter of water contains approximately 10^{23} individual atoms, most of which are only of 2 types and we are certain that *all* of them are from only a few hundred possibilities. Clearly, the universe is almost, but not quite, a single thing - or nothing.

This uniformity permits measurement of astounding precision - often far beyond what could be reasonably expected from the physical scales for which our theories were originally developed.

The search for gravitational waves is one such experiment. Gravitational waves are perturbations of space time metric and are a direct consequence of Einstein's equation describing classical gravitation. They are extremely hard to generate - to the degree that originally there was doubt as to whether they exist at all and are not a mathematical artifact of general relativity.

Nevertheless, with time we gained more confidence in the accuracy of general relativity and now have indirect confirmation of the existence of gravitational waves

from a binary pulsar system [1] which shows decreases in the orbital period matching the calculated energy loss from gravitational radiation.

LIGO is an experiment to detect gravitational waves directly by comparing distances in two perpendicular directions. It has now reached the sensitivity that puts us at the threshold of discovering gravitational radiation - provided there is a convenient astronomical source nearby.

One class of such sources is a rotating neutron star which is expected to emit continuous gravitational signals. We have performed a search for such sources and established upper limits which are presented here.

The previous searches for continuous signals have included a long coherence search for known pulsars ([2], [3] and [4]), a short period coherent method targeted Scorpius X-1 in selected bands and performed an all-sky search in 160-768 Hz band ([5]). A long period semi-coherent method was used for an all-sky search in 200-400 Hz band. A hierarchical coherent search Einstein@Home running on the BOINC infrastructure ([6]) has performed blind all-sky searches on S4 and S5 data ([7] and [8]).

PowerFlux, described in this thesis, has appeared first in the paper [9] together with two other semi-coherent searches (Hough, Stackslide). A comparison of sensitivities was made which established that PowerFlux is more sensitive in well-behaving regions of frequency space. A subsequent paper [10] described application of PowerFlux to S5 data and the results of detection search. These results are presented in chapter IV.

The signals we search for are extremely weak and require long integration times. Thus our results are limited by computational resources and interferometer sensitivity. While the former can be partially overcome with more sophisticated algorithms and larger computer clusters, improving the latter requires changes in the instrument

itself.

To aid the latter cause we present a prototype for a wavefront camera capable of sampling a laser beam wavefront at a rate of 100 million samples per second, which we hope will serve as a powerful instrument for gravitational wave interferometers.

CHAPTER II

Gravitational waves

The derivation of gravitational waves from the Einstein equation can be found in the literature, for example [11] or [12].

The general form of a gravitational-wave signal is usually described in terms of two orthogonal transverse polarizations defined as "+" with waveform $h_+(t)$ and "×" with waveform $h_\times(t)$. The calibrated response seen by an interferometric gravitational-wave detector is then [14]

$$h(t) = F_+(t, \alpha, \delta, \psi)h_+(t) + F_\times(t, \alpha, \delta, \psi)h_\times(t), \tag{2.1}$$

where t is time in the detector frame, α is the source right ascension, δ is the source declination, ψ is the polarization angle of the wave, and $F_{+,\times}$ are the detector antenna pattern functions for the two orthogonal polarizations. For periodic (nearly pure sinusoidal) gravitational waves, which in general are elliptically polarized, the individual components $h_{+,\times}$ have the form

$$h_+(t) = A_+ \cos\Phi(t), \tag{2.2}$$

$$h_\times(t) = A_\times \sin\Phi(t), \tag{2.3}$$

where A_+ and $A_\times$ are the amplitudes of the two polarizations, and $\Phi(t)$ is the phase of the signal at the detector.

For completeness, we will present a derivation of gravitational waves in a slightly more general form than commonly used, by taking the cosmological constant into account and allowing for a non-flat underlying metric. We will then assure ourselves that the frequency drift caused by the resulting extra terms will not cause a problem in our analysis.

2.1 Starting point

The Einstein equation in free space is given by:

$$R_{\mu\nu} - \frac{1}{2} g_{\mu\nu} R + g_{\mu\nu}\Lambda = 0$$

Here we assume that our metric has signature $(-,+,+,+)$.

Taking the trace of the above, we obtain

$$R = 4\Lambda$$

which, after substitution, yields an equivalent, but simpler equation:

$$R_{\mu\nu} = g_{\mu\nu}\Lambda$$

We will assume that the metric tensor $\tilde{g}_{\mu\nu}$ is a sum of background metric $g_{\mu\nu}$ and perturbation $h_{\mu\nu}$:

$$\tilde{g}_{\mu\nu} = g_{\mu\nu} + h_{\mu\nu}$$

The inverse gives a metric tensor that acts on covariant forms:

$$\tilde{g}^{\mu\nu} = g^{\mu\nu} - g^{\mu\alpha} h_{\alpha\beta} g^{\beta\nu} + g^{\mu\alpha} h_{\alpha\beta} g^{\beta\gamma} h_{\gamma\delta} g^{\delta\nu} + O(h^3)$$

In this formula, as well as others in this paper, we use Einstein's convention that repeated indices are summed over.

The Christoffel symbols describe the unique torsion-free connection compatible with the metric and are given by:

$$\Gamma^{\gamma}_{\alpha\beta} = \frac{1}{2} g^{\delta\gamma} \left(\frac{\partial}{\partial x^{\alpha}} g_{\delta\beta} + \frac{\partial}{\partial x^{\beta}} g_{\alpha\delta} - \frac{\partial}{\partial x^{\delta}} g_{\alpha\beta} \right)$$

Lowering the upper index provides a convenient expression linear in the metric:

$$\Gamma_{\alpha\beta\gamma}(g) = \frac{1}{2} \left(\frac{\partial}{\partial x^{\alpha}} g_{\gamma\beta} + \frac{\partial}{\partial x^{\beta}} g_{\alpha\gamma} - \frac{\partial}{\partial x^{\gamma}} g_{\alpha\beta} \right)$$

It is also convenient to compute

$$\Gamma^{\beta}_{\alpha\beta} = \frac{1}{2} g^{\delta\beta} \frac{\partial}{\partial x^{\alpha}} g_{\delta\beta} = \frac{1}{2} \frac{\partial}{\partial x^{\alpha}} \log\det \|g_{\delta\beta}\|$$

The Ricci curvature tensor is the trace of the Riemann curvature tensor:

$$\begin{aligned} R_{\alpha\beta} &= R^{\gamma}{}_{\alpha\gamma\beta} = \underbrace{\frac{\partial \Gamma^{\gamma}_{\alpha\beta}}{\partial x^{\gamma}} - \frac{\partial \Gamma^{\gamma}_{\alpha\gamma}}{\partial x^{\beta}}}_{A} + \underbrace{\Gamma^{\gamma}_{\alpha\beta}\Gamma^{\delta}_{\gamma\delta} - \Gamma^{\delta}_{\alpha\gamma}\Gamma^{\gamma}_{\beta\delta}}_{B} \\ &= \underbrace{\frac{\partial \left(g^{\gamma\delta}\Gamma_{\alpha\beta\delta} \right)}{\partial x^{\gamma}} - \frac{\partial \left(g^{\gamma\delta}\Gamma_{\alpha\gamma\delta} \right)}{\partial x^{\beta}}}_{A} + \underbrace{g^{\delta\xi} g^{\gamma\mu} \Gamma_{\alpha\beta\gamma}\Gamma_{\mu\delta\xi} - g^{\delta\xi} g^{\gamma\mu} \Gamma_{\alpha\mu\delta}\Gamma_{\beta\delta\xi}}_{B} \end{aligned}$$

2.2 Einstein manifolds

The solutions to the equation $R_{\mu\nu} = g_{\mu\nu}\Lambda$ are known as Einstein manifolds. Their full classification is not known which makes analysis difficult. As an example and to show that such manifolds exist we will classify metrics that are conformally equivalent to the standard Minkowski metric. The solution includes constant spacetime and anti de Sitter spaces.

Let $g_{\mu\nu} = f\eta_{\mu\nu}$ where f is a scalar function and $\eta_{\mu\nu}$ is the standard flat metric. Then

$$\begin{aligned} \Gamma^{\gamma}_{\alpha\beta} &= \tfrac{1}{2} \tfrac{\eta^{\delta\gamma}}{f} \left(\tfrac{\partial f}{\partial x^{\alpha}} \eta_{\delta\beta} + \tfrac{\partial f}{\partial x^{\beta}} \eta_{\alpha\delta} - \tfrac{\partial f}{\partial x^{\delta}} \eta_{\alpha\beta} \right) \\ &= \tfrac{1}{2} \left(\tfrac{\partial \log f}{\partial x^{\alpha}} \delta^{\gamma}_{\beta} + \tfrac{\partial \log f}{\partial x^{\beta}} \delta^{\gamma}_{\alpha} - \eta^{\delta\gamma} \tfrac{\partial \log f}{\partial x^{\delta}} \eta_{\alpha\beta} \right) \end{aligned}$$

$$\Gamma^{\beta}_{\alpha\beta} = 2\frac{\partial \log f}{\partial x^{\alpha}}$$

The Ricci tensor is equal to

$$R_{\alpha\beta} \;=\; R^{\gamma}{}_{\alpha\gamma\beta} = \underbrace{\frac{\partial \Gamma^{\gamma}_{\alpha\beta}}{\partial x^{\gamma}} - \frac{\partial \Gamma^{\gamma}_{\alpha\gamma}}{\partial x^{\beta}}}_{A} + \underbrace{\Gamma^{\gamma}_{\alpha\beta}\Gamma^{\delta}_{\gamma\delta} - \Gamma^{\delta}_{\alpha\gamma}\Gamma^{\gamma}_{\beta\delta}}_{B}$$

The $A_{\alpha\beta}$ terms are the exterior derivative, while the $B_{\alpha\beta}$ is the commutator.

$$\begin{aligned} A_{\alpha\beta} &= \tfrac{\partial \Gamma^{\gamma}_{\alpha\beta}}{\partial x^{\gamma}} - \tfrac{\partial \Gamma^{\gamma}_{\alpha\gamma}}{\partial x^{\beta}} \\ &= \tfrac{\partial^2 \log f}{\partial x^{\alpha}\partial x^{\beta}} - \tfrac{1}{2}\eta^{\delta\gamma}\tfrac{\partial^2 \log f}{\partial x^{\delta}\partial x^{\gamma}}\eta_{\alpha\beta} - 2\tfrac{\partial^2 \log f}{\partial x^{\alpha}\partial x^{\beta}} \\ &= -\tfrac{\partial^2 \log f}{\partial x^{\alpha}\partial x^{\beta}} - \tfrac{1}{2}\eta^{\delta\gamma}\tfrac{\partial^2 \log f}{\partial x^{\delta}\partial x^{\gamma}}\eta_{\alpha\beta} \end{aligned}$$

$$\begin{aligned} B_{\alpha\beta} &= \Gamma^{\gamma}_{\alpha\beta}\Gamma^{\delta}_{\gamma\delta} - \Gamma^{\delta}_{\alpha\gamma}\Gamma^{\gamma}_{\beta\delta} \\ &= 2\tfrac{\partial \log f}{\partial x^{\alpha}}\tfrac{\partial \log f}{\partial x^{\beta}} - \eta^{\delta\gamma}\tfrac{\partial \log f}{\partial x^{\delta}}\tfrac{\partial \log f}{\partial x^{\gamma}}\eta_{\alpha\beta} - \\ &\quad -\tfrac{1}{4}\left(\tfrac{\partial \log f}{\partial x^{\alpha}}\delta^{\delta}_{\gamma} + \tfrac{\partial \log f}{\partial x^{\gamma}}\delta^{\delta}_{\alpha} - \eta^{\delta\mu}\tfrac{\partial \log f}{\partial x^{\mu}}\eta_{\alpha\gamma}\right)\left(\tfrac{\partial \log f}{\partial x^{\delta}}\delta^{\gamma}_{\beta} + \tfrac{\partial \log f}{\partial x^{\beta}}\delta^{\gamma}_{\delta} - \eta^{\mu\gamma}\tfrac{\partial \log f}{\partial x^{\mu}}\eta_{\delta\beta}\right) \\ &= 2\tfrac{\partial \log f}{\partial x^{\alpha}}\tfrac{\partial \log f}{\partial x^{\beta}} - \eta^{\delta\gamma}\tfrac{\partial \log f}{\partial x^{\delta}}\tfrac{\partial \log f}{\partial x^{\gamma}}\eta_{\alpha\beta} - \\ &\quad -\tfrac{1}{4}\left(2\tfrac{\partial \log f}{\partial x^{\alpha}}\tfrac{\partial \log f}{\partial x^{\beta}} - \eta^{\delta\gamma}\tfrac{\partial \log f}{\partial x^{\delta}}\tfrac{\partial \log f}{\partial x^{\gamma}}\eta_{\alpha\beta} + 4\tfrac{\partial \log f}{\partial x^{\alpha}}\tfrac{\partial \log f}{\partial x^{\beta}} - \eta^{\delta\gamma}\tfrac{\partial \log f}{\partial x^{\delta}}\tfrac{\partial \log f}{\partial x^{\gamma}}\eta_{\alpha\beta}\right) \\ &= \tfrac{1}{2}\tfrac{\partial \log f}{\partial x^{\alpha}}\tfrac{\partial \log f}{\partial x^{\beta}} - \tfrac{1}{2}\eta^{\delta\gamma}\tfrac{\partial \log f}{\partial x^{\delta}}\tfrac{\partial \log f}{\partial x^{\gamma}}\eta_{\alpha\beta} \end{aligned}$$

Thus

$$R_{\alpha\beta} \;=\; -\tfrac{\partial^2 \log f}{\partial x^{\alpha}\partial x^{\beta}} - \tfrac{1}{2}\eta^{\delta\gamma}\tfrac{\partial^2 \log f}{\partial x^{\delta}\partial x^{\gamma}}\eta_{\alpha\beta} + \tfrac{1}{2}\tfrac{\partial \log f}{\partial x^{\alpha}}\tfrac{\partial \log f}{\partial x^{\beta}} - \tfrac{1}{2}\eta^{\delta\gamma}\tfrac{\partial \log f}{\partial x^{\delta}}\tfrac{\partial \log f}{\partial x^{\gamma}}\eta_{\alpha\beta} = f\Lambda\eta_{\alpha\beta}$$

For $\alpha \neq \beta$ the flat metric $\eta_{\alpha\beta}$ vanishes yielding a simple equation:

$$\frac{\partial^2 \log f}{\partial x^{\alpha}\partial x^{\beta}} - \frac{1}{2}\frac{\partial \log f}{\partial x^{\alpha}}\frac{\partial \log f}{\partial x^{\beta}} = 0$$

Differentiating the logarithm produces:

$$\frac{\frac{\partial^2 f}{\partial x^{\alpha}\partial x^{\beta}}f - \frac{\partial f}{\partial x^{\alpha}}\frac{\partial f}{\partial x^{\beta}}}{f^2} - \frac{1}{2}\frac{\frac{\partial f}{\partial x^{\alpha}}\frac{\partial f}{\partial x^{\beta}}}{f^2} = 0$$

which simplifies to

$$\frac{\partial^2 f}{\partial x^\alpha \partial x^\beta} f - \frac{3}{2} \frac{\partial f}{\partial x^\alpha} \frac{\partial f}{\partial x^\beta} = 0$$

that easily integrates:

$$\frac{\frac{\partial^2 f}{\partial x^\alpha \partial x^\beta}}{\frac{\partial f}{\partial x^\beta}} = \frac{3}{2} \frac{\frac{\partial f}{\partial x^\alpha}}{f}$$

We find

$$\frac{\partial f}{\partial x^\beta} = \sqrt{f^3} C_1(x^\beta)$$

which integrates to

$$f = \frac{1}{\left(\sum_\alpha y^\alpha(x^\alpha)\right)^2} \tag{2.4}$$

where y^α are some functions of x^α alone.

The above derivation used the fact that $\eta_{\alpha\beta}$ is diagonal and constant. However, this leaves a fairly large group of spacetime transformations intact - namely translations and rotations from $O(k, n-k)$. A solution of the form 2.4 obtained in one coordinate system should still have the same form when acted on by a translation or a rotation.

This places severe constraints on functions $y^\alpha(x^\alpha)$ - they could be at most quadratic, with quadratic term being an invariant of $O(k, n-k)$:

$$y^\alpha(x^\alpha) = A\eta_{\alpha\alpha} \left(x^\alpha\right)^2 + B_\alpha x^\alpha + C_\alpha$$

By using translations and rotations this general form can be reduced to one of three possibilities:

- $f = A$ - we have a plain flat metric, $\Lambda = 0$.
- $f = A/\left(x^{\alpha_0}\right)^2$ for a specific index α_0. This includes anti-deSitter space with negative Λ.

- $f = A/\left(\eta_{\alpha\beta}x^\alpha x^\beta + B\right)^2$

We will now verify that these satisfy the case $\alpha = \beta$ and find how Λ depends on constants A and B.

Instead of substituting directly, it is convenient to compute derivatives of the general expression of f first:

$$\begin{aligned}
\frac{\partial f}{\partial x^\alpha} &= -2\sqrt{f^3}\frac{\partial y^\alpha}{\partial x^\alpha} \\
\frac{\partial \log f}{\partial x^\alpha} &= -2\sqrt{f}\frac{\partial y^\alpha}{\partial x^\alpha} \\
\frac{\partial^2 \log f}{\partial^2 x^\alpha} &= -2\sqrt{f}\frac{\partial^2 y^\alpha}{(\partial x^\alpha)^2} + 2f\left(\frac{\partial y^\alpha}{\partial x^\alpha}\right)^2
\end{aligned}$$

Now let us set $\alpha = \beta$ and substitute f into the Einstein equation:

$$\begin{aligned}
R_{\alpha\alpha} &= 2\sqrt{f}\frac{\partial^2 y^\alpha}{(\partial x^\alpha)^2} - 2f\left(\frac{\partial y^\alpha}{\partial x^\alpha}\right)^2 + \sqrt{f}\eta_{\alpha\alpha}\textstyle\sum_\gamma \eta^{\gamma\gamma}\frac{\partial^2 y^\gamma}{(\partial x^\gamma)^2} - f\eta_{\alpha\alpha}\sum_\gamma \eta^{\gamma\gamma}\left(\frac{\partial y^\gamma}{\partial x^\gamma}\right)^2 \\
&\quad +2f\left(\frac{\partial y^\alpha}{\partial x^\alpha}\right)^2 - 2f\eta_{\alpha\alpha}\textstyle\sum_\gamma \eta^{\gamma\gamma}\left(\frac{\partial y^\gamma}{\partial x^\gamma}\right)^2 \\
&= 2\sqrt{f}\frac{\partial^2 y^\alpha}{(\partial x^\alpha)^2} + \sqrt{f}\eta_{\alpha\alpha}\textstyle\sum_\gamma \eta^{\gamma\gamma}\frac{\partial^2 y^\gamma}{(\partial x^\gamma)^2} - 3f\eta_{\alpha\alpha}\sum_\gamma \eta^{\gamma\gamma}\left(\frac{\partial y^\gamma}{\partial x^\gamma}\right)^2 = f\Lambda\eta_{\alpha\alpha}
\end{aligned}$$

It is now easy to substitute particular values of $y^\alpha(x^\alpha)$:

- $f = A$ - all derivatives vanish, $\Lambda = 0$ as expected.
- $f = A/\left(x^{\alpha_0}\right)^2$ for one value of α_0 and zero for others. We find $\Lambda = -\frac{3\eta^{\alpha_0\alpha_0}}{A}$. The sign of the cosmological constant depends on whether we chose time or space variable x^{α_0}. In the latter case the constant is negative (assuming positive A) which exactly matches anti-deSitter space.
- $f = A/\left(\eta_{\alpha\beta}x^\alpha x^\beta + B\right)^2$. Substituting we find:

$$\begin{aligned}
R_{\alpha\alpha} &= \frac{4}{\eta_{\alpha\beta}x^\alpha x^\beta + B}\eta_{\alpha\alpha} + \frac{8}{\eta_{\alpha\beta}x^\alpha x^\beta + B}\eta_{\alpha\alpha} - \frac{12}{\left(\eta_{\alpha\beta}x^\alpha x^\beta + B\right)^2}\eta_{\alpha\alpha}\eta_{\alpha\beta}x^\alpha x^\beta \\
&= \frac{12B}{A}f\eta_{\alpha\alpha}
\end{aligned}$$

The cosmological constant is thus equal to $\Lambda = \frac{12B}{A}$.

2.3 Perturbation

We easily find that the perturbed connection has the following expansion:

$$\begin{aligned}\tilde{\Gamma}^{\gamma}_{\alpha\beta} &= \Gamma^{\gamma}_{\alpha\beta} - g^{\gamma\delta}h_{\delta\mu}\Gamma^{\mu}_{\alpha\beta} + \\ &\quad + \tfrac{1}{2}g^{\delta\gamma}\left(\tfrac{\partial}{\partial x^{\alpha}}h_{\delta\beta} + \tfrac{\partial}{\partial x^{\beta}}h_{\alpha\delta} - \tfrac{\partial}{\partial x^{\delta}}h_{\alpha\beta}\right) \\ &= \Gamma^{\gamma}_{\alpha\beta} - g^{\gamma\delta}h_{\delta\mu}\Gamma^{\mu}_{\alpha\beta} + g^{\delta\gamma}\Gamma_{\alpha\beta\delta}(h)\end{aligned}$$

To simplify our notation we introduce the tensor $h^{\beta}_{\alpha} = g^{\alpha\mu}h_{\mu\beta}$. The above equation can then be written as:

$$\tilde{\Gamma}^{\gamma}_{\alpha\beta} = \Gamma^{\gamma}_{\alpha\beta} - h^{\gamma}_{\mu}\Gamma^{\mu}_{\alpha\beta} + g^{\gamma\delta}\Gamma_{\alpha\beta\delta}(h)$$

In particular

$$\tilde{\Gamma}^{\beta}_{\alpha\beta} = \Gamma^{\beta}_{\alpha\beta} - h^{\beta}_{\mu}\Gamma^{\mu}_{\alpha\beta} + \tfrac{1}{2}g^{\beta\delta}\tfrac{\partial}{\partial x^{\alpha}}h_{\delta\beta}$$

To compute the Ricci tensor we will now transition to a geodesic coordinate system with respect to metric $g_{\alpha\beta}$ around a particular point p. In that point Christoffel symbols and partial derivatives of the metric tensor vanish and Ricci tensor consists of A terms only:

$$R^{\delta}{}_{\alpha\gamma\beta}(p) = \tfrac{\partial\Gamma^{\delta}_{\alpha\beta}}{\partial x^{\gamma}} - \tfrac{\partial\Gamma^{\delta}_{\alpha\gamma}}{\partial x^{\beta}}$$

$$R_{\alpha\beta}(p) = \frac{\partial\Gamma^{\gamma}_{\alpha\beta}(p)}{\partial x^{\gamma}} - \frac{\partial\Gamma^{\gamma}_{\alpha\gamma}(p)}{\partial x^{\beta}}$$

The perturbed Christoffel symbols are:

$$\tilde{\Gamma}^{\gamma}_{\alpha\beta}(p) = g^{\gamma\delta}\Gamma_{\alpha\beta\delta}(h)$$

The perturbed Ricci tensor is computed as follows:

$$\begin{aligned}\tilde{A}_{\alpha\beta}(p) &= \tfrac{\partial\tilde{\Gamma}^{\gamma}_{\alpha\beta}}{\partial x^{\gamma}} - \tfrac{\partial\tilde{\Gamma}^{\gamma}_{\alpha\gamma}}{\partial x^{\beta}} \\ &= \tfrac{\partial\Gamma^{\gamma}_{\alpha\beta}}{\partial x^{\gamma}} - \tfrac{\partial\Gamma^{\gamma}_{\alpha\gamma}}{\partial x^{\beta}} - h^{\gamma}_{\mu}\left(\tfrac{\partial\Gamma^{\mu}_{\alpha\beta}}{\partial x^{\gamma}} - \tfrac{\partial\Gamma^{\mu}_{\alpha\gamma}}{\partial x^{\beta}}\right) + \\ &\quad + g^{\gamma\delta}\left(\tfrac{\partial\Gamma_{\alpha\beta\delta}(h)}{\partial x^{\gamma}} - \tfrac{\partial\Gamma_{\alpha\gamma\delta}(h)}{\partial x^{\beta}}\right)\end{aligned}$$

$$\begin{aligned}\tilde{B}_{\alpha\beta}(p) &= \tilde{\Gamma}^{\gamma}_{\alpha\beta}\tilde{\Gamma}^{\delta}_{\gamma\delta} - \tilde{\Gamma}^{\delta}_{\alpha\gamma}\tilde{\Gamma}^{\gamma}_{\beta\delta} \\ &= g^{\gamma\delta}\Gamma_{\alpha\beta\delta}(h)g^{\mu\delta}\Gamma_{\gamma\mu\delta}(h) - g^{\mu\delta}\Gamma_{\alpha\gamma\delta}(h)g^{\gamma\nu}\Gamma_{\beta\mu\nu}(h) = 0\end{aligned}$$

$$\tilde{R}_{\alpha\beta}(p) = R_{\alpha\beta}(p) - h^{\gamma}_{\mu}R^{\mu}{}_{\alpha\gamma\beta}(p) + g^{\gamma\delta}\left(\frac{\partial\Gamma_{\alpha\beta\delta}(h)}{\partial x^{\gamma}} - \frac{\partial\Gamma_{\alpha\gamma\delta}(h)}{\partial x^{\beta}}\right)$$

The last term involves second order derivatives:

$$\begin{aligned}g^{\gamma\delta}\left(\frac{\partial\Gamma_{\alpha\beta\delta}(h)}{\partial x^{\gamma}} - \frac{\partial\Gamma_{\alpha\gamma\delta}(h)}{\partial x^{\beta}}\right) &= \tfrac{1}{2}g^{\gamma\delta}\left(\left(\frac{\partial^2 h_{\delta\beta}}{\partial x^{\alpha}\partial x^{\gamma}} + \frac{\partial^2 h_{\alpha\delta}}{\partial x^{\beta}\partial x^{\gamma}} - \frac{\partial^2 h_{\alpha\beta}}{\partial x^{\delta}\partial x^{\gamma}}\right) - \right. \\ &\quad \left. - \left(\frac{\partial^2 h_{\delta\gamma}}{\partial x^{\alpha}\partial x^{\beta}} + \frac{\partial^2 h_{\alpha\delta}}{\partial x^{\gamma}\partial x^{\beta}} - \frac{\partial^2 h_{\alpha\gamma}}{\partial x^{\delta}\partial x^{\beta}}\right)\right) \\ &= \tfrac{1}{2}g^{\gamma\delta}\left(\frac{\partial^2 h_{\delta\beta}}{\partial x^{\alpha}\partial x^{\gamma}} - \frac{\partial^2 h_{\alpha\beta}}{\partial x^{\delta}\partial x^{\gamma}} - \frac{\partial^2 h_{\delta\gamma}}{\partial x^{\alpha}\partial x^{\beta}} + \frac{\partial^2 h_{\alpha\gamma}}{\partial x^{\delta}\partial x^{\beta}}\right) \\ &= \tfrac{1}{2}g^{\gamma\delta}\left(\nabla_{\alpha}\nabla_{\gamma}h_{\delta\beta} - \nabla_{\delta}\nabla_{\gamma}h_{\alpha\beta} - \nabla_{\alpha}\nabla_{\beta}h_{\delta\gamma} + \nabla_{\delta}\nabla_{\beta}h_{\alpha\gamma}\right)\end{aligned}$$

Thus we obtain:

$$\tilde{R}_{\alpha\beta} = R_{\alpha\beta} - h^{\gamma}_{\mu}R^{\mu}{}_{\alpha\gamma\beta} + \tfrac{1}{2}g^{\gamma\delta}\left(\nabla_{\alpha}\nabla_{\gamma}h_{\delta\beta} - \nabla_{\delta}\nabla_{\gamma}h_{\alpha\beta} - \nabla_{\alpha}\nabla_{\beta}h_{\delta\gamma} + \nabla_{\delta}\nabla_{\beta}h_{\alpha\gamma}\right)$$

We are now in position to substitute into Einstein's equation:

$$\begin{aligned}0 &= \tilde{R}_{\alpha\beta} - \tilde{g}_{\alpha\beta}\Lambda = \\ &= -h^{\gamma}_{\mu}R^{\mu}{}_{\alpha\gamma\beta} + \tfrac{1}{2}g^{\gamma\delta}\left(\nabla_{\alpha}\nabla_{\gamma}h_{\delta\beta} - \nabla_{\delta}\nabla_{\gamma}h_{\alpha\beta} - \nabla_{\alpha}\nabla_{\beta}h_{\delta\gamma} + \nabla_{\delta}\nabla_{\beta}h_{\alpha\gamma}\right) - h_{\alpha\beta}\Lambda\end{aligned}$$

We rewrite this as

$$\nabla_{\gamma}\nabla^{\gamma}h_{\alpha\beta} + \nabla_{\alpha}\nabla_{\beta}h^{\gamma}_{\gamma} - \nabla_{\beta}\nabla^{\gamma}h_{\alpha\gamma} - \nabla_{\alpha}\nabla^{\gamma}h_{\gamma\beta} + 2h_{\alpha\beta}\Lambda + 2h^{\gamma}_{\mu}R^{\mu}{}_{\alpha\gamma\beta} = 0 \tag{2.5}$$

Before proceeding further we would like to transform the second term into a form that will prove easier to handle. This is commonly done by introducing the trace-reversed tensor $\bar{h}$:

$$\bar{h}_{\alpha\beta} = h_{\alpha\beta} - \frac{1}{2}h^{\gamma}_{\gamma}g_{\alpha\beta}$$

That one needs to do this becomes clear only after attempting some calculations - or after consulting books on the subject. The reason has likely something to do with

the fact that conformal transformations form a group and it is thus convenient to factor out its action.

We obtain

(2.6)

$$\nabla_\gamma\nabla^\gamma\bar{h}_{\alpha\beta}-\nabla_\beta\nabla^\gamma\bar{h}_{\alpha\gamma}-\nabla_\alpha\nabla^\gamma\bar{h}_{\gamma\beta}+2\bar{h}_{\alpha\beta}\Lambda-2g_{\alpha\beta}\bar{h}^\delta_\delta\Lambda+2\bar{h}^\gamma_\mu R^\mu{}_{\alpha\gamma\beta}+\frac{1}{2}g_{\alpha\beta}\nabla^\gamma\nabla_\gamma h^\delta_\delta=0$$

To deal with the last term recall that $R=4\Lambda$ and its variation is thus zero which provides a constraint on $h_{\alpha\beta}$:

$$\tilde{R}-R=-h^\gamma_\mu R^\mu{}_{\alpha\gamma\beta}g^{\alpha\beta}+\left(\nabla^\alpha\nabla^\beta h_{\alpha\beta}-\nabla^\delta\nabla_\delta h^\alpha_\alpha\right)-R^{\alpha\beta}h_{\alpha\beta}=0$$

which yields:

$$\frac{1}{2}\nabla_\gamma\nabla^\gamma h^\alpha_\alpha=\nabla^\alpha\nabla^\beta\bar{h}_{\alpha\beta}-R^{\alpha\beta}\bar{h}_{\alpha\beta}-\bar{h}^\gamma_\mu R^\mu{}_{\alpha\gamma\beta}g^{\alpha\beta}+R\bar{h}^\alpha_\alpha$$

Remembering that $R_{\alpha\beta}=g_{\alpha\beta}\Lambda$ this simplifies to

$$\frac{1}{2}\nabla_\gamma\nabla^\gamma h^\alpha_\alpha=\nabla^\alpha\nabla^\beta\bar{h}_{\alpha\beta}-\bar{h}^\gamma_\mu R^\mu{}_{\alpha\gamma\beta}g^{\alpha\beta}+3\Lambda\bar{h}^\alpha_\alpha$$

Substituting into equation 2.6 and grouping similar terms, we obtain:

(2.7)
$$\begin{aligned}\nabla_\gamma\nabla^\gamma\bar{h}_{\alpha\beta}-\nabla_\beta\nabla^\gamma\bar{h}_{\alpha\gamma}-\nabla_\alpha\nabla^\gamma\bar{h}_{\gamma\beta}+g_{\alpha\beta}\nabla^\gamma\nabla^\delta\bar{h}_{\gamma\delta}+\\ +2\bar{h}_{\alpha\beta}\Lambda+2\bar{h}^\gamma_\mu R^\mu{}_{\alpha\gamma\beta}-g_{\alpha\beta}\left(\bar{h}^\nu_\mu R^\mu{}_{\gamma\nu\delta}g^{\gamma\delta}-\Lambda\bar{h}^\gamma_\gamma\right)=0\end{aligned}$$

This equation admits many solutions that are merely the result of a change of coordinates. These "gauge" degrees of freedom are convenient to factor out.

Suppose that we have a flow generated by the vector field ξ^α. This flow acts on the metric tensor as

$$L_\xi g_{\alpha\beta}=\xi^\gamma\nabla_\gamma g_{\alpha\beta}+g_{\alpha\gamma}\nabla_\beta\xi^\gamma+g_{\gamma\beta}\nabla_\alpha\xi^\gamma$$

The first term vanishes as the covariant derivative commutes with the metric tensor it is compatible with. If $h_{\alpha\beta}$ is a solution of equation 2.5, then

$$h_{\alpha\beta}+g_{\alpha\gamma}\nabla_\beta\xi^\gamma+g_{\gamma\beta}\nabla_\alpha\xi^\gamma$$

is a solution that is diffeomorphic to the original $h_{\alpha\beta}$. In terms of trace-reversed tensor, the new solution is

$$\bar{h}_{\alpha\beta} + g_{\alpha\gamma}\nabla_\beta\xi^\gamma + g_{\gamma\beta}\nabla_\alpha\xi^\gamma - g_{\alpha\beta}\nabla_\gamma\xi^\gamma$$

By focusing on a particular class of diffeomorphic solution, we can simplify the equation for $\bar{h}_{\alpha\beta}$. Let us require that $\nabla^\beta\bar{h}_{\alpha\beta} = 0$ which would eliminate three terms with partial derivatives. This condition is usually called transverse or Lorentz gauge in literature. This can be achieved as long as the following equation has a solution ξ:

$$\nabla^\beta\nabla_\beta\xi_\alpha = -\nabla^\beta\bar{h}_{\alpha\beta} \tag{2.8}$$

Fortunately, this is an inhomogeneous wave equation in ξ which possesses a solution for reasonably well-behaved metric $g_{\alpha\beta}$ and right hand side term. In particular, the solution exists for non-degenerate metrics close to the Lorentz metric with very mild conditions on the regularity of terms (such as differentiability) - which can be relaxed by use of Sobolev spaces.

Thus, in the Lorentz gauge $\nabla^\beta\bar{h}_{\alpha\beta} = 0$ we have the following equation for the trace-reversed perturbation $\bar{h}_{\alpha\beta}$:

$$\nabla_\gamma\nabla^\gamma\bar{h}_{\alpha\beta} + 2\bar{h}_{\alpha\beta}\Lambda + 2\bar{h}^\gamma_\mu R^\mu{}_{\alpha\gamma\beta} - g_{\alpha\beta}\left(\bar{h}^\nu_\mu R^\mu{}_{\gamma\nu\delta}g^{\gamma\delta} - \Lambda\bar{h}^\gamma_\gamma\right) = 0 \tag{2.9}$$

This equation is clearly a wave equation in $h_{\alpha\beta}$ with (possibly direction dependent) mass terms contributed by the cosmological constant and the Riemann tensor of the underlying metric.

2.4 Form of expected signals

2.4.1 Polarizations

For the case of a flat underlying metric (which implies $\Lambda = 0$) one easily finds solutions of the form

$$\bar{h}_{\alpha\beta} = H_{\alpha\beta} e^{ik_\mu x^\mu}$$

with the following equations on k and H:

$$\begin{cases} H_{\alpha\beta} k_\mu k^\mu = 0 \\ H_{\alpha\beta} k^\beta = 0 \end{cases}$$

Assuming non-trivial perturbation, we have $k_\mu k^\mu = 0$. The Lorentz gauge equation 2.8 still has some remaining freedom, as ξ is determined up to an arbitrary solution ϕ of the homogeneous part. Picking it as $\phi_\alpha = v_\alpha e^{ik_\mu x^\mu}$ we find

$$H_{\alpha\beta} \to H_{\alpha\beta} + ik_\beta v_\alpha + ik_\alpha v_\beta - ig_{\alpha\beta} k^\gamma v_\gamma$$

Let us fix a timelike vector u that has a non-zero scalar product with k. Representing v_α as $\lambda u_\alpha + v^0_\alpha$, where $k^\alpha v^0_\alpha = 0$ we obtain:

$$H_{\alpha\beta} \to H_{\alpha\beta} + i\lambda(u_\alpha k_\beta + k_\alpha u_\beta - g_{\alpha\beta} k^\gamma u_\gamma) + i(v^0_\alpha k_\beta + ik_\alpha v^0_\beta)$$

The trace of the second term is then $-2i\lambda k^\alpha u_\alpha$, and one can pick λ to null out the trace of $H_{\alpha\beta}$. The freedom in v^0_α can be used to set $H_{\alpha\beta} u^\beta = 0$ as the condition $H_{\alpha\beta} k^\beta = 0$ insures the equation

$$v^0_\alpha k_\beta u^\beta + ik_\alpha v^0_\beta u^\beta = -iH_{\alpha\beta} u^\beta + \lambda k_\alpha u^\beta u_\beta$$

is solvable.

We can then pick a coordinate system where u is the time coordinate and k has

only time and z-axis components. Then $H_{\alpha\beta}$ has the following form:

$$H = \begin{pmatrix} 0 & 0 & 0 & 0 \\ 0 & H_{xx} & H_{xy} & 0 \\ 0 & H_{xy} & -H_{xx} & 0 \\ 0 & 0 & 0 & 0 \end{pmatrix}$$

which clearly exhibits two polarization components called "plus" and "cross".

2.4.2 Generation of gravitational waves

While most accelerated movement of physical objects generate gravitational waves, the waves are too weak to be detected by our instruments. The most likely sources of observable waves are thought to be astrophysical in origin. In LIGO's band of interest the expected sources of continuous waves are rotating neutron stars.

Neutron stars are extremely dense objects that have undergone gravitational collapse, but were just shy of the mass necessary to form a black hole. The momentum imparted by the progenitor star induces a very high spin rate - with the highest currently known value of 716 Hz ([15]).

A spinning neutron star can potentially produce gravitational waves via several mechanisms: it can have a non-axisymmetric distribution of mass, it could be precessing or it could have excited r-modes ([5]). In all of these cases it is thought that the leading terms should be quadrupolar in origin with lower order terms suppressed by conservation of mass and momentum.

A quadrupolar source possesses an axis along which it emits circularly polarized waves, while the waves emitted in the plane perpendicular to this axis are linearly polarized.

The polarization of the waves as received by the observer is thus dependent on the inclination angle ι of this axis. In situation where this axis is tilted, there is

an additional angle ψ that determines the mix of plus and cross polarizations. The detector on Earth thus observes plane waves with the following amplitudes:

$$\begin{aligned} h_+ &= \tfrac{1}{2} h_0 \left(1 + \cos^2 \iota\right), \\ h_\times &= h_0 \cos \iota \end{aligned}$$

For a blind search we do not know the orientation of potential sources and must thus maximize over ι and ψ. This invariably leads to dominance of linear polarizations in determining upper limits, as they contribute the smallest amount of power to the detector.

2.4.3 Possible deviations from classical wave equation

We have seen above that in the case of flat metric and zero cosmological constant gravitational waves obey the same wave equation as electromagnetic radiation, and have two polarizations.

We will now address the question of how much does the assumption of flat metric and zero cosmological constant influence a search for continuous waves.

Such a search typically involves integration over prolonged periods and is very sensitive to small corrections to frequency. For example, in case of the PowerFlux search (described in detail later) the frequency resolution is typically 0.55 mHz which constitutes less than 0.4 parts per million at 1500 Hz. For coherent searches the frequency resolution is even greater.

The potential influence of the mass terms can be manifested in two ways: as a correction term to the magnitude of the Doppler shift and as a shift in phase of the signal. In both cases we are concerned with the relative size of the correction to the signal frequency. In addition, the blind searches would only be impacted by time-dependent corrections, as constant shifts in frequency will not preclude a detection.

Current measurements ([16]) restrict the cosmological constant to be below $10^{-52}\mathrm{m}^{-2} = \left(3\times10^{-18}\mathrm{Hz}\cdot c^{-1}\right)^2$ which will not impact any of the current LIGO searches which cover the frequency between 50 Hz and 1500 Hz.

The Riemann tensor of a Schwarzschild solution has terms of the order of $\frac{r_s}{r^3}$, where r_s is the Schwarzschild radius and $r \gg r_s$. For the Earth's surface (where LIGO interferometers are located) this number is below $\left(3\times10^{-6}\ \mathrm{Hz}\cdot c^{-1}\right)^2$ and does not affect current searches.

An additional concern, relevant for searches that take timing from electromagnetic observations, is whether the redshift experienced by electromagnetic and gravitational waves is the same or not, especially in view of mass-like terms appearing in equation 2.9.

Suppose that the metric is static, i.e. it does not have components that depend on time (both Schwarzschild or Kerr metrics possess this property). Then the wave equation for either gravitational or electromagnetic waves will not have any t-dependent terms either and will have the form:

$$\left(A(x^k)\frac{\partial^2}{\partial t^2} + B\left(x^k, \frac{\partial}{\partial x^k}\right)\frac{\partial}{\partial t} + C\left(x^k, \frac{\partial}{\partial x^k}\right)\right)\Psi = 0$$

which allows the time and space coordinates to separate via the usual ansatz $\Psi = e^{i\omega t}X(x^k)$. Thus, in this coordinate system, the frequency of the wave is constant throughout its region of propagation and only the velocity changes.

Of course, the frequency measured in the proper time can vary, but the conversion from the above coordinate system to the proper time does not depend on the character of the propagating wave. Thus, even though the equations for electromagnetic and gravitational waves differ they will experience exactly the same redshift in any static solutions of the Einstein equations, though their phase relation will, in general, vary from one location in space to another due to different space dependent terms.

We conclude that at the present sensitivities of searches for gravitational waves one can use the approximation of a regular wave equation and, in particular, the Dopper shifts and the redshift can be computed the same as for electromagnetic radiation.

CHAPTER III

Detectors

Figure 3.1: LIGO Hanford Observatory (credit: LIGO Laboratory).

LIGO H1, H2 (located in Hanford, WA,figure 3.1) and L1 (located in Livingston, LA, see [22]) are interferometric detectors that measure strain (relative length difference) induced by gravitational waves via comparison of lengths of two perpendicular arms. The desired sensitivity is on the order of 10^{-21} which presents a number of challenges.

These detectors consist of two evacuated tubes 4 km in length (2 km for H2) that enclose Fabry-Perot cavities. The distance measurement is made by the laser beam travelling between large 25cm mirrors (figure 3.2) acting as free-falling masses

Figure 3.2: One of the mirrors in its suspension (credit: LIGO Laboratory).

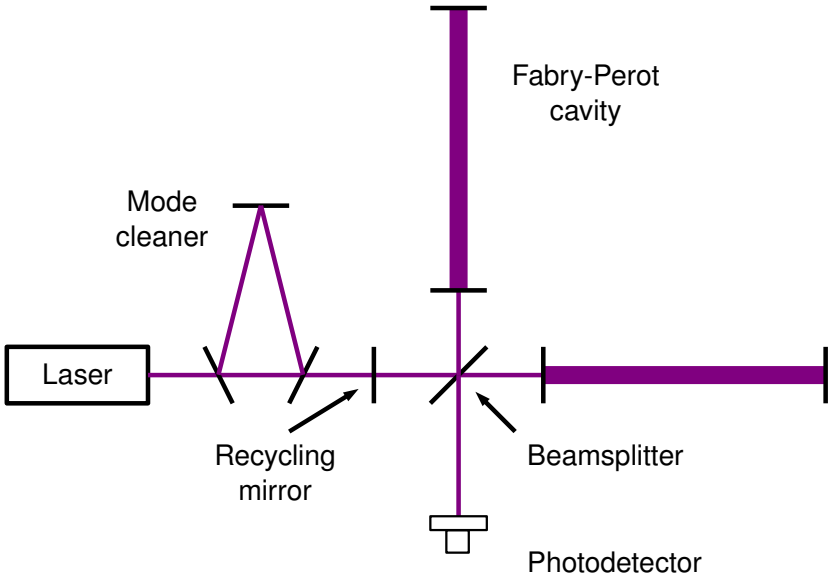

Figure 3.3: Schematic of Initial LIGO interferometer

along the cavity axis. The beams exiting the optical cavities are compared in a Michelson-Morley interferometer with an output photodiode (figure 3.3).

A good introduction to interferometric gravitational wave detectors can be found in [13], and a detailed description of the Initial LIGO instrument can be found in [22].

3.1 Broadband noise sources

There are several major contributors to measurement noise. Seismic noise is particularly pronounced at low frequencies and is mitigated by a multi-stage mechanical isolation system that includes both passive and active components.

Middle frequencies are, in general, strongly affected by thermal noise from mirrors and their suspensions. The mirrors and their suspension wires (or fibers) perform as elastic mechanical oscillators of particularly narrow resonances (high Q). The current material of choice is silica (SiO_2), but sapphire (Al_2O_3) has also been explored and will in fact be used by an upcoming Japanese detector (which, in addition, will cool the mirrors to cryogenic temperature, see [23]).

Lastly, the high frequencies are dominated by shot noise from individual photons striking the mirrors. To mitigate this noise, the power circulating in the cavities is large with present values in 10-20kW range.

3.2 Narrowband noise sources

Narrowband noise sources affect only a small fraction of the spectrum, but they complicate analysis a good deal by introducing non-Gaussianity into local spectral bands, mimicking real signals. We have listed some sources[1] in table 3.1.

[1] The width column refers to affected spectrum band of **demodulated** continuous wave gravitational wave signals, not the spectrum space of interferometer

Frequency Hz	Spindown Hz/s	Width[1] Hz	Description
×60.00	NA	1.25	power lines and their harmonics
46.70	NA	0.1	H1 calibration line
54.70	NA	0.1	L1 calibration line
265.58	-4.15×10^{-12}	0.1	injected pulsar 0
849.06	-3.00×10^{-10}	1	injected pulsar 1
575.16	-1.37×10^{-13}	0.5	injected pulsar 2
108.86	-1.46×10^{-17}	0.1	injected pulsar 3
1401.55	-2.54×10^{-8}	0.5	injected pulsar 4
52.80	-4.03×10^{-18}	0.1	injected pulsar 5
148.29	-6.73×10^{-9}	2	injected pulsar 6
1220.90	-1.12×10^{-9}	0.2	injected pulsar 7
193.75	-8.65×10^{-9}	1.25	injected pulsar 8
763.85	-1.40×10^{-17}	0.1	injected pulsar 9
128.00	NA	0.1	128 Hz - a strong 16 Hz harmonic
256.10	NA	0.25	256 Hz - a strong 16 Hz harmonic
350.00	NA	20	suspension mode
393.10	NA	0.25	H1 calibration line
396.70	NA	0.25	L1 calibration line
1144.30	NA	0.25	H1 calibration line
1151.91	NA	0.25	L1 calibration line

Table 3.1: Sources of narrowband noise

Power mains spectral lines (60 Hz in North America), including sidebands, typically extend 1.25 Hz in each direction and make semi-coherent analysis impractical in these narrow bands because of highly non-Gaussian, elevated noise levels. This contamination requires excluding 5% of the spectrum. Unfortunately, the Crab pulsar rotational frequency is 29.78 Hz, which places it in the excluded area: $2\nu = 59.56$ Hz. A fully coherent search, which is less susceptible to 60 Hz contamination, has been carried out in [24].

Mirrors, suspensions and other interferometer components have internal vibration modes that can couple to the gravitation wave channel. For example, suspension wires create strong noise in $330 - 370$ Hz area and its harmonics.

Calibration lines - hardware injected signals used to gauge interferometer sensitivity - and simulated pulsars (discussed below) can show up as noise. In particular, injected signal 8 has a very large spindown, making it span a range of frequencies.

Digital electronics can contribute relatively weak, well localized (to a mHz level) spikes. For example, during LIGO's fourth science run a GPS clock was responsible for a frequency comb with 1 Hz periodicity.

3.3 Science runs

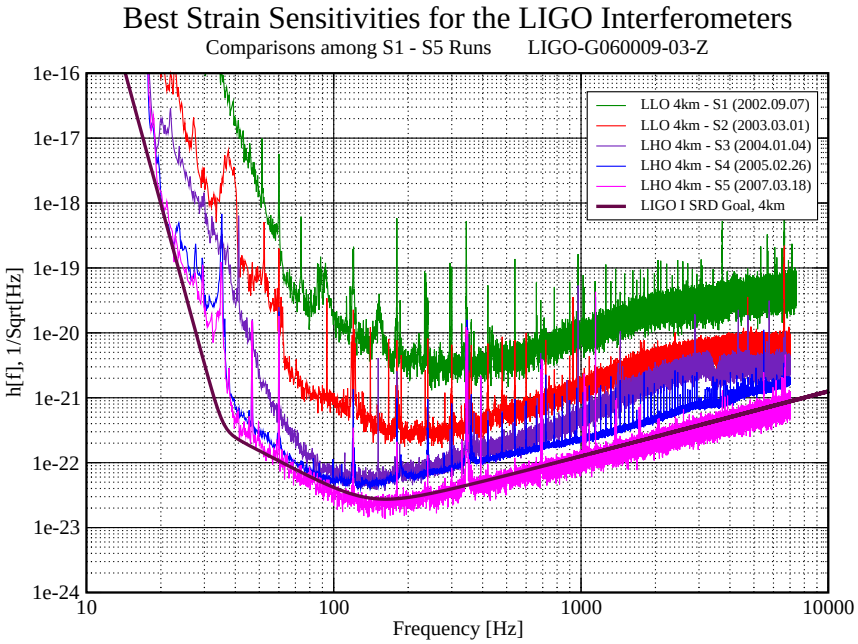

Figure 3.4: Interferometer improvement between science runs. The solid black curve is the design goal for interferometers.

The development of LIGO detectors has been marked by periods of active commissioning, where potentially disruptive changes in detector configuration can be implemented, interspersed with time dedicated to acquiring scientific data. The latter periods are usually called "science runs" and are denoted by the letter S followed by a number. The progress from S1 through S5 (and currently running S6) has seen dramatic improvements in detector sensitivity and stability (figure 3.4).

In the following chapter (IV) we will describe searches for continuous gravitational

Parameter	S4	S5
Start time	2005-02-22 12:00 (CST)	2005-11-04 16:00 (UTC) [2]
End time	2005-03-23 00:00 (CST)	2007-10-01 00:00 (UTC)
Timebase	29.5 days	$\approx$ 2 years
Triple coincident time	$\approx$ 15 days	$\approx$ 1 year
Sensitivity at 150 Hz	6.3×10^{-23} Hz$^{-1/2}$	2.8×10^{-23} Hz$^{-1/2}$

Table 3.2: S4 and S5 science run parameters

waves in data taken during the fourth and fifth science runs, the most sensitive to date. Table 3.2 shows when the runs occurred and their best attained sensitivities. The triple coincident time is important for searches looking for transient events and is indicative of detector stability. The timebase describes the time period spanned by the data and thus the fraction of Earth orbit traversed during this time. This influences the contribution of Doppler shifts from Earth orbital velocity vector to distinguishing true continuous signals from detector artifacts.

During the run a number of hardware injections were made (see table 3.3) which provide an end-to-end test of data acquisition and analysis infrastructure. The injections are performed by introducing simulated signal data into the servo control loop, which then causes test masses to move as if the signals were caused by the gravitational wave.

These injections require knowledge of the detector response in real time and thus the actual injected strain amplitudes have slight differences among LIGO's three interferometers because of imperfect calibration knowledge at the time of the injection. The last two simulated pulsars listed are binary system injections with additional orbital parameters that are not shown. The searches described in chapter IV use some of these hardware injected signals for validation of the analysis pipeline. More extensive software injections into the already acquired data are also used for high-statistics evaluation of pipeline performance.

Index	f_0 (Hz)	df/dt (Hz s^{-1})	RA (rad)	DEC (rad)	ψ (rad)	A_+	$A_\times$
0	265.57693	-4.15×10^{-12}	1.2488	−0.9812	0.77	4.03×10^{-25}	3.92×10^{-25}
1	849.07086	-3.00×10^{-10}	0.6526	−0.5140	0.36	2.58×10^{-24}	1.97×10^{-24}
2	575.16357	-1.37×10^{-13}	3.7569	0.0601	−0.22	7.48×10^{-24}	-7.46×10^{-24}
3	108.85716	-1.46×10^{-17}	3.1132	−0.5836	0.44	1.64×10^{-23}	-2.63×10^{-24}
4	1402.11049	-2.54×10^{-08}	4.8867	−0.2176	−0.65	2.46×10^{-22}	1.27×10^{-22}
5	52.80832	-4.03×10^{-18}	5.2818	−1.4633	−0.36	5.89×10^{-24}	4.49×10^{-24}
6	148.44006	-6.73×10^{-09}	6.2614	−1.1418	0.47	1.42×10^{-24}	-4.26×10^{-25}
7	1220.93316	-1.12×10^{-09}	3.8995	−0.3569	0.51	1.04×10^{-23}	9.98×10^{-24}
8	193.94977	-8.65×10^{-09}	6.1329	−0.5833	0.17	1.60×10^{-23}	2.35×10^{-24}
9	763.84732	-1.45×10^{-17}	3.4712	1.3210	−0.01	5.62×10^{-24}	-5.03×10^{-24}
10	501.23897	-7.03×10^{-16}	3.1132	−0.5836	0.44	6.55×10^{-23}	-1.05×10^{-24}
11	376.07013	-4.26×10^{-15}	6.1329	−0.5833	0.17	2.62×10^{-22}	-4.20×10^{-23}

Table 3.3: Nominal (intended) parameters for hardware injected signals for GPS reference time 793130413 s (start of S4 run).

CHAPTER IV

Search for continuous gravitational waves in LIGO S4 and S5 data

4.1 PowerFlux

As its name suggests, the PowerFlux program estimates the incoming power of gravitational radiation from particular directions in the sky. The Doppler frequency modulations caused by Earth motion provides most of the discriminating power, with detector orientation ("antenna response") contributing in a strong but directionally coarse manner.

We have applied this program to data collected by the LIGO instrument network during the S4 run [9] and the first nine months of the S5 run [10] - analysis of the full S5 data is currently in progress.

A detailed description of PowerFlux and usage manual is contained in [20] and a comparison to alternative semi-coherent methods can be found in [9], which, in particular, show PowerFlux to have better sensitivity in well-behaved regions of frequency spectrum.

The computational requirements of PowerFlux can be described as moderate - a typical all-sky search over multiple spindowns requires a few months of cluster time to complete. This is as compared to light weight targeted searches that finish in the matter of days or compute-intensive Einstein@Home that runs on tens of thousands

of computers for several months.

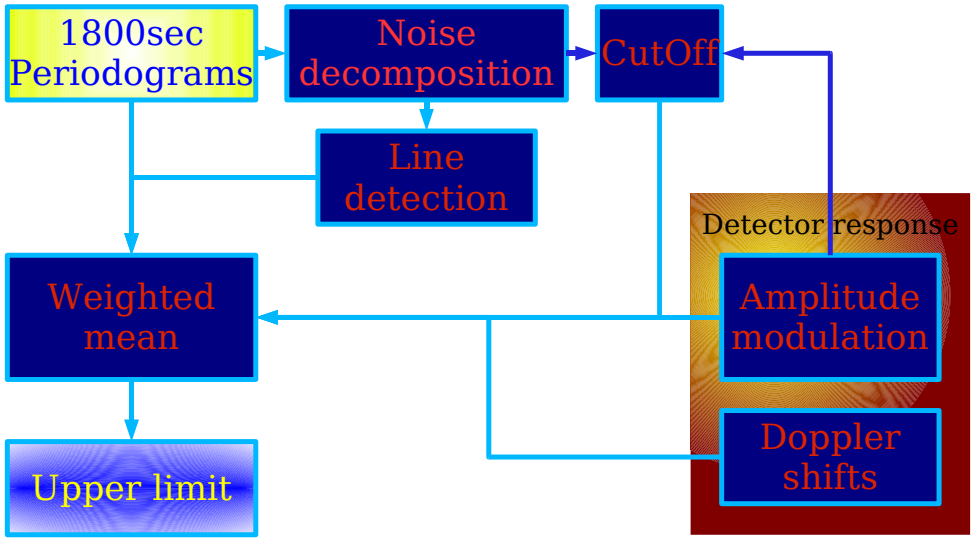

Figure 4.1: PowerFlux flowchart

The PowerFlux analysis (see figure 4.1) starts by partitioning science mode time domain data $h(t)$ into 30 minute segments with 50% overlap. The $h(t)$ dataset is synthesized from data recorded during the run (see [19]) and covers the frequency range from 30 Hz to 3000 Hz. Each segment is then Hann-windowed and subjected to a Fourier transform. The resulting SFTs ("short" Fourier transforms) are stored on disk. To speed up analysis, they can be distributed to individual nodes of a computing cluster and, optionally, "striped" - converted from a one segment/all frequencies format to a one frequency band/many segments format. The former technique was employed in the early S5 analysis ([10]).

Each PowerFlux instance loads the data for the frequency band of interest. The loading process is controlled by a datasets description file (an example is shown in figure 4.2).

The datasets description consists of one or more sections describing a subset of

```
new_dataset "H1_test1"
detector "LHO"
gaussian_fill 793154935 3600 4001 1e-24
apply_hanning_filter

# Arguments: gps_start gps_stop ref_time strain frequency spindown ra dec iota psi phi
#
inject_cw_signal -1 -1 793154935 2e-23 100.1389 -1e-8 2.0 1.0 1.570796 0.392699 0.0

-------------------------------------------------------------------------------

new_dataset "July_H1_1800SFT_v1C03hoftHann"
detector "LHO"
#gps_start 816069857
expand_sft_array 11598
dc_factor 1.074
segments_file "/home/volodya/July.followup/S5.v3.data/segments.July.H1.txt"
file "H-S5_H1_October-815494281-62550760.sft"

new_dataset "July_L1_1800SFT_v1C03hoftHann"
detector "LLO"
#gps_start 816069857
expand_sft_array 8198
dc_factor 0.96
segments_file "/home/volodya/July.followup/S5.v3.data/segments.July.L1.txt"
file "L-S5_L1_October-816070133-61868157.sft"
```

Figure 4.2: Simulated datasets description file, followed by an example of a file used in S5 analysis

SFTs to load and qualify for further analysis. Data from different detectors are always separated into different subsets. In addition, one might want to create different datasets for periods when interferometer had different noise floor. It is convenient to visualize the data loaded from a single subset as a matrix with time and frequency dimensions.

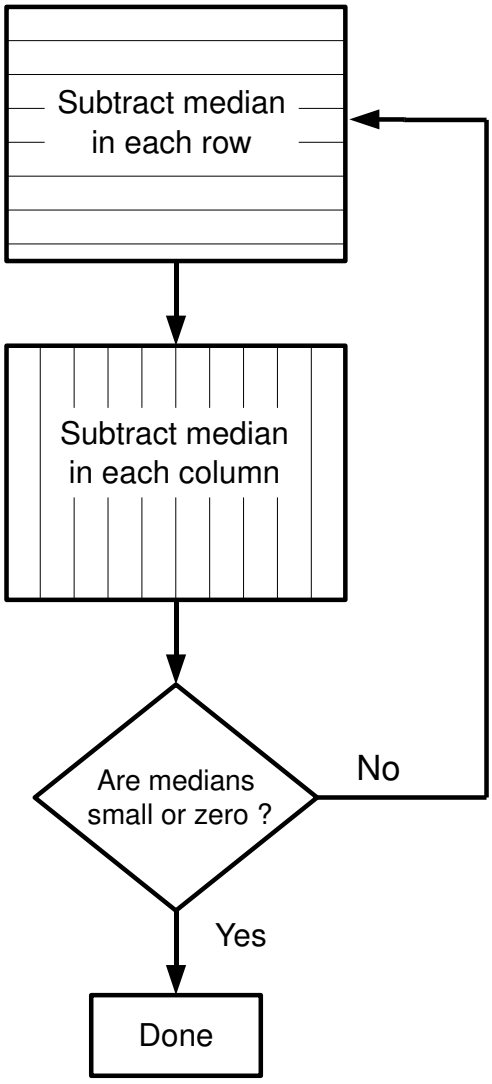

Figure 4.3: Noise decomposition algorithm

The SFTs from each dataset are subjected to noise decomposition that separates the strain powers into time-dependent (called TMedians) and frequency-dependent (FMedians) contributions, with the residuals having a zero median along time and along frequency dimensions.

$$\log_{10}\left(\text{Power}(t,f)\right) = \text{TMedian}(t) + \text{FMedian}(f) + \text{Res}(t,f)$$

The algorithm (see figure 4.3) has a remarkable property of always converging in a finite number of steps for matrices of odd dimensions. In practice, the convergence is extremely rapid for matrices of any size, with 10-15 steps sufficient to reach precision limits of the floating point data type.

Figures 4.4 and 4.5 show example plots of TMedians and FMedians for hardware injected signal 2. Since the signal was pulsed on and off during the run, the TMedian plot x axis (labeled in hours since the beginning of the run) shows gaps. The y axis of the plots shows logarithm of power after subtracting a normalization constant that is necessary to prevent underflow of 32 bit real number data type. The x axis of the FMedian plot shows frequency in Hz.

The expected signal contributes to only a few frequency bins in each SFTs and thus constitutes a very small proportion of the entire dataset. The histogram of the residuals (figure 4.6) is thus quite stable against injections of small to moderate strengths. The deviations of the usual shape of this histogram can thus be used to flag bands which possess disturbed data. Such deviations are typically due to detector artifacts that change their frequency ("wander") during the run and can also include particularly loud hardware injected signals (such injected signal 3 and 8).

The SFTs are then analyzed to determine average noise level and sharp "line" artifacts - large excesses of power confined to a few neighboring frequency bins. At

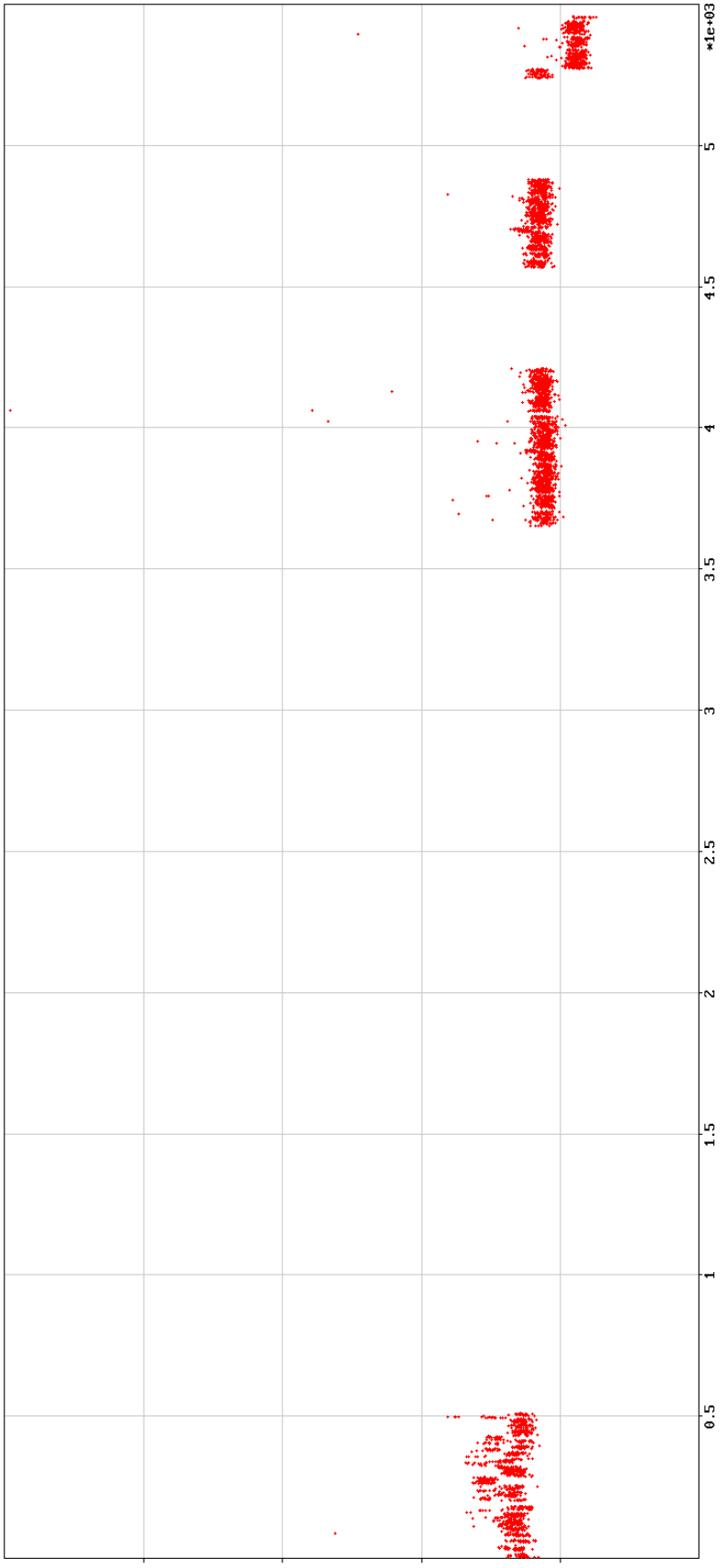

Figure 4.4: Example of TMedians - time dependent contribution to background noise. The large gaps show periods when hardware injected signal was off during the run.

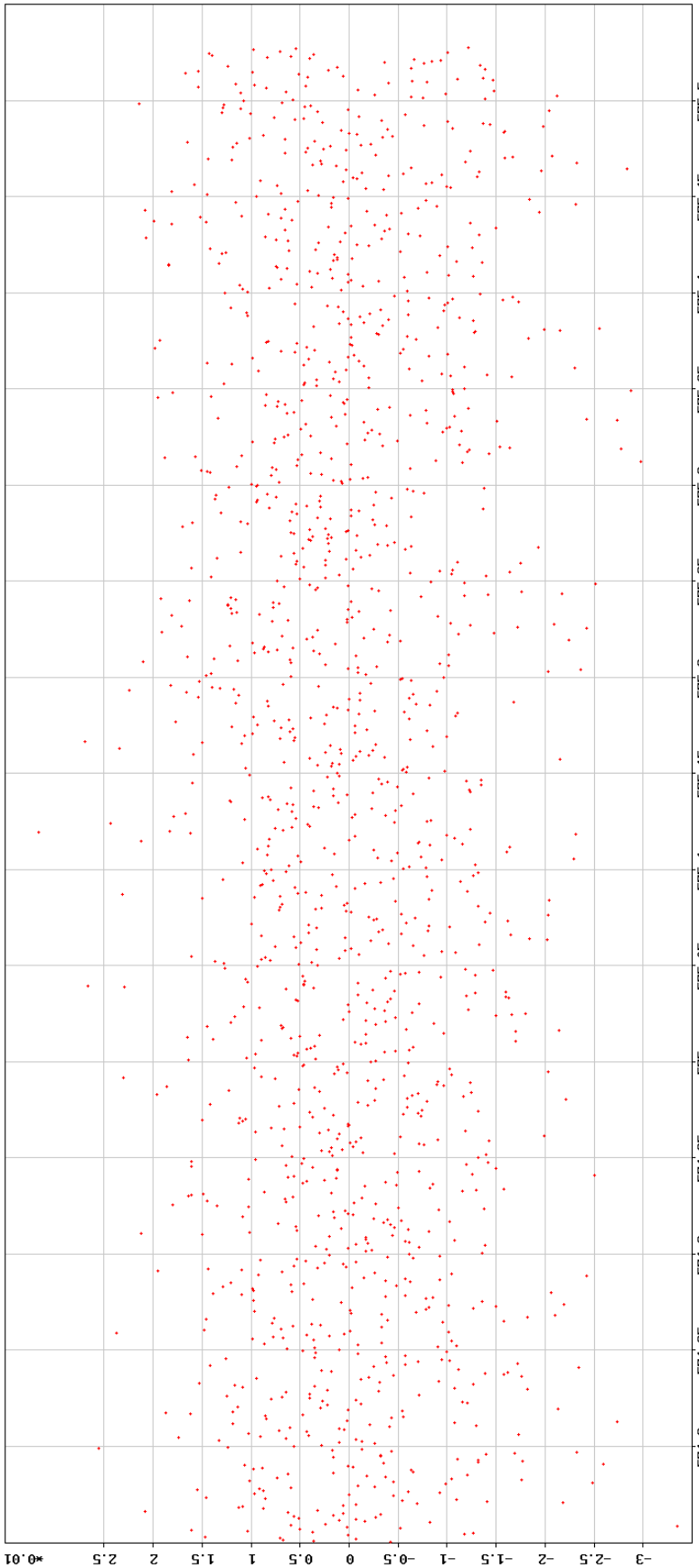

Figure 4.5: Example of FMedians - frequency dependent contribution to background noise

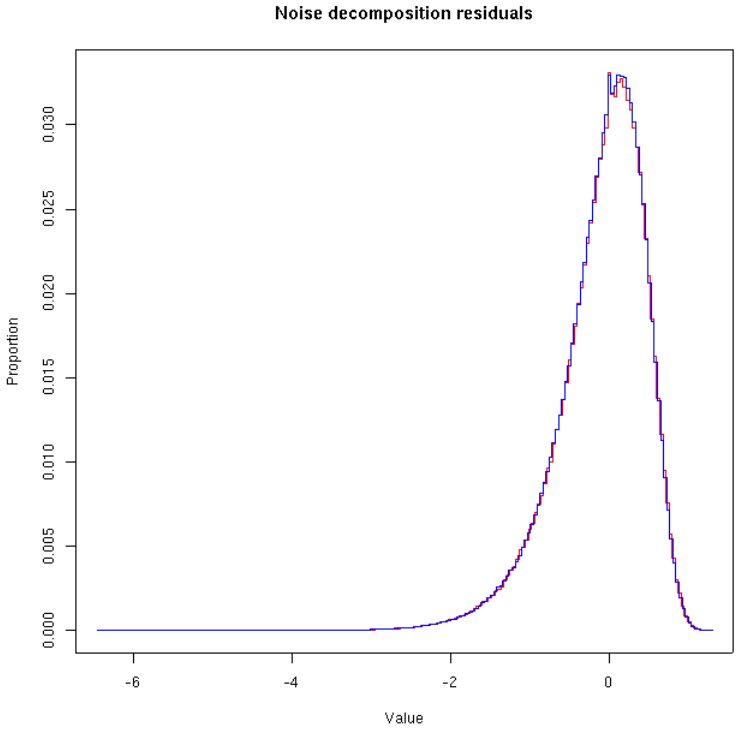

Figure 4.6: Noise decomposition residuals. Blue curve shows results of analysis of hardware injected pulsar signal. Red curve shows analysis of simulated noise SFTs produced with pseudo-random generator.

most 5 of such artifacts are flagged during analysis and, when line veto is enabled, the power from these frequency bins is not included in power sums, with corresponding reduction in weight. This can lead to some (usually small - this strongly depends on the timebase of the run) portions of sky contain frequency bins with particularly small weight. This is undesirable, as even though the power sum is still perfectly valid, a large reduction in weight leads to corresponding increase in error of the results. Compared to their neighbours these frequency bins can then look like large artifacts, resulting in large upper limits and spurious high-SNR outliers. To deal with this, we employ a configurable cutoff (usually set at 20%), below which the affected sky templates are completely excluded from the analysis.

Next, for any particular sky location we compute Doppler corrections and antenna pattern coefficients, as well as "spindown" frequency shifts - a linear function of time meant to account for slow changes in source frequency. These are applied to a narrow band of frequency space consisting of 501 bins spanning a 0.25-Hz band to provide a vector of power sums. The number of bins was chosen to be high enough to yield good statistics for background estimation while assuring an approximately white (flat) spectrum in most searched bands. Additionally we wanted to avoid known 1-Hz artifacts in a significant proportion of analyzed frequency space which affected S4 and earlier science runs and were caused by imperfect data acquisition electronics.

During S4 and S5 analysis the antenna pattern coefficients were computed for 4 linear polarizations offset by $\frac{\pi}{8}$ from each other and for a circular polarization. The former polarizations produce the worst case upper limit, while the latter samples a high-sensitivity region of parameter space.

The weighted power sums are computed according to the formula

$$\mathrm{PSum}_k(i) = \sum_t \frac{w_k(t)}{W_k} \frac{P(i,t)}{A_k(t)}$$

where $w_k(t)$ are the time dependent weights for polarization number k, $W_k = \sum_t w_k(t)$ is the total weight and $P(i,t)$ denotes power in bin i of SFT obtained at time t. $A_k(t)$ stands for amplitude response at time t.

The antenna pattern coefficients and noise decomposition data, computed previously, are used to establish power sum weights and cutoff values that define weights too small to make a significant contribution. This results in significant savings of computing resources. For example, the time to compute a power sum for a single linear polarization is approximately half of the time spent on computing a circular polarization sum.

The weights used are

$$w_k(t) = A_k(t)^2 10^{-2\mathrm{TMedian}(t)}$$

i.e. the inverse square (up to a constant) of standard deviation of sum components $P(i,t)/A_k(t)$. This results in the smallest possible standard deviation of the power sum $\mathrm{PSum}_k(i)$ (see [20]).

Having obtained a vector of strain power sums, it is analyzed for power excess (possibly indicating a presence of a signal) using the Feldman-Cousins algorithm [21] and for compliance with Gaussian noise, using the Kolmogorov-Smirnov test with in-sample estimation of normal distribution parameters. High values of the Kolmogorov-Smirnov statistic are usually due to detector artifacts, especially very sharp spectral features.

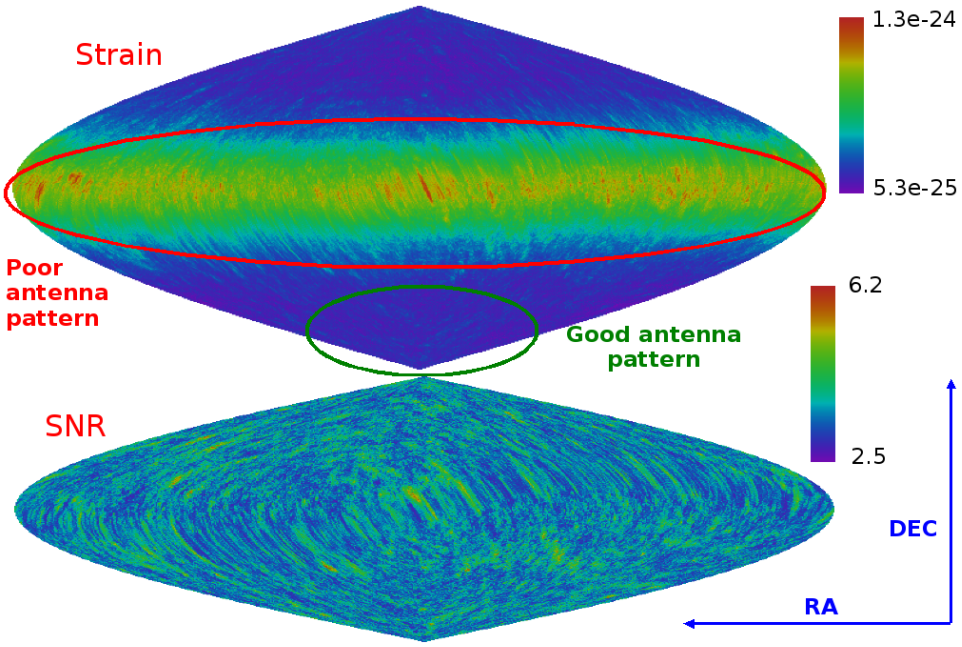

Figure 4.7: Typical sky dependence of upper limits due to antenna pattern.

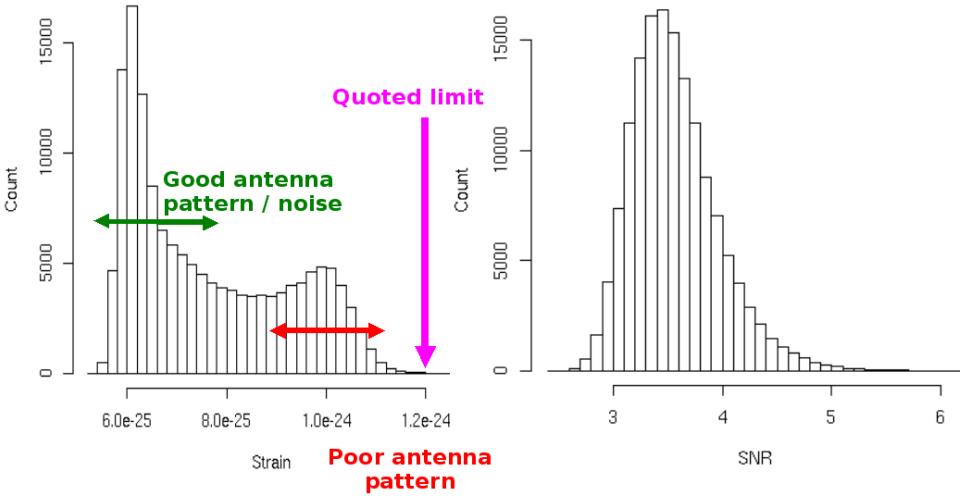

Figure 4.8: Distribution of upper limits and signal to noise ratios.

4.2 Setting of upper limits

During operation, PowerFlux produces a local upper limit on strain power and maximum signal-to-noise ratio for each 0.25 Hz band, given a particular sky location, spindown and orientation parameters. For ease of understanding, this data is reduced by maximizing over polarizations, sky locations or frequencies and then written into log files, binary files and plots. For upper limits it makes sense to report separately worst-case results (linear polarizations) and best-case results (circular polarization).

The average upper limit value can vary greatly over the sky. This variation is largely dependent on detector declination, though some diurnal variance is present as well, especially for short data runs (see figure 4.7). Signal-to-noise ratios do not exhibit this dependence.

For publication the results are further reduced by computing maximums over sky locations in a large area. This maximum is significantly larger than the average value, as illustrated in figure 4.8.

At this moment we have published results from two science runs: S4 [9] and early S5 [10].

4.3 Validation

The correctness of the PowerFlux pipeline has been checked in multiple ways:

- The code contains internal diagnostics that serve both to validate portions of the PowerFlux code and as a check that compilation went correctly.
- We have performed numerous software injection runs, where the simulated signal was added to interferometer data or to pseudo-random Gaussian noise. These checks were done both using internal signal injection code and using external,

independently written tools.

- An analysis of hardware injected signals was carried out, which provided an end-to-end pipeline test.
- A line-by-line review of PowerFlux code was conducted by scientists outside of the continuous waves working group.

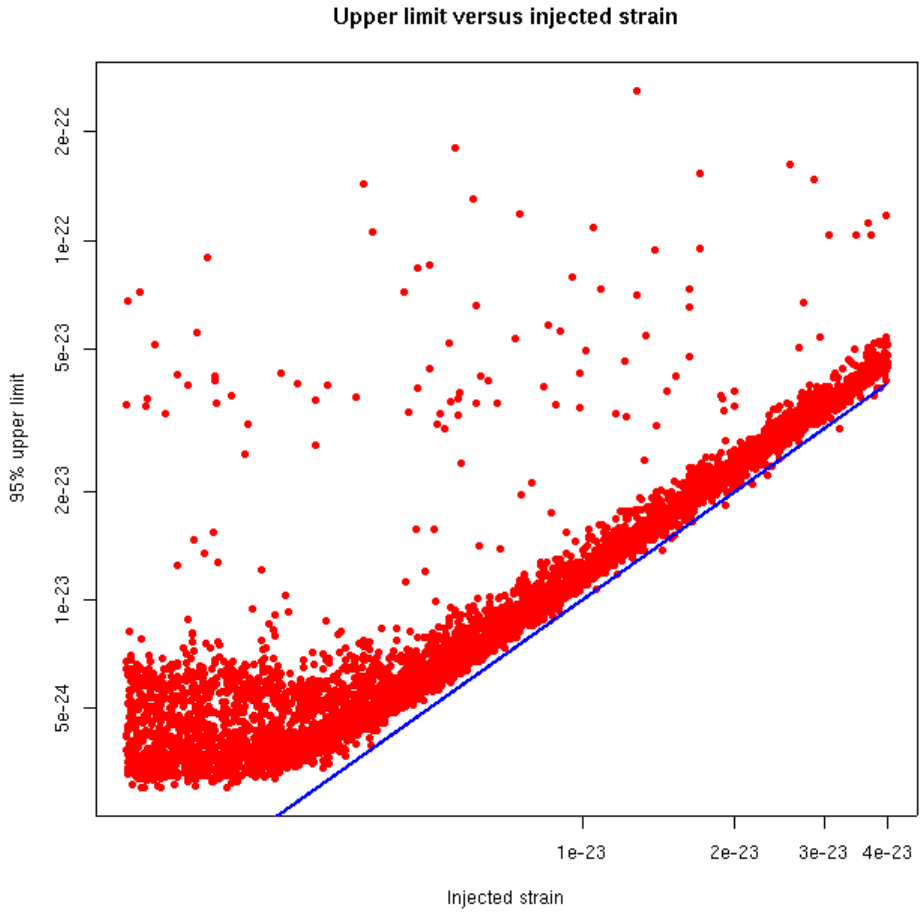

Figure 4.9: Upper limit versus injected strain

Figure 4.9 shows results of one of the earliest Monte-Carlo runs. It consisted of 8000 software injections in the 200-300 Hz frequency band with locations uniformly distributed on the sky. The orientations of the injected signals were fixed to be linear,

as this provides the smallest amount of power to the detector. The reconstructed upper limits are almost always above the blue curve of injected signal strain, providing 96.3% frequentist success rate. This number was computed from data depicted on the figure excluding region on the left that shows points with injected strains below or close to background level.

Multiple such runs were performed for each analysis in order to validate changes to the code, to assure correct behaviour of the algorithms dealing with detector artifacts, to determine run parameters such as spindown stepping and to establish coincidence criteria between interferometers.

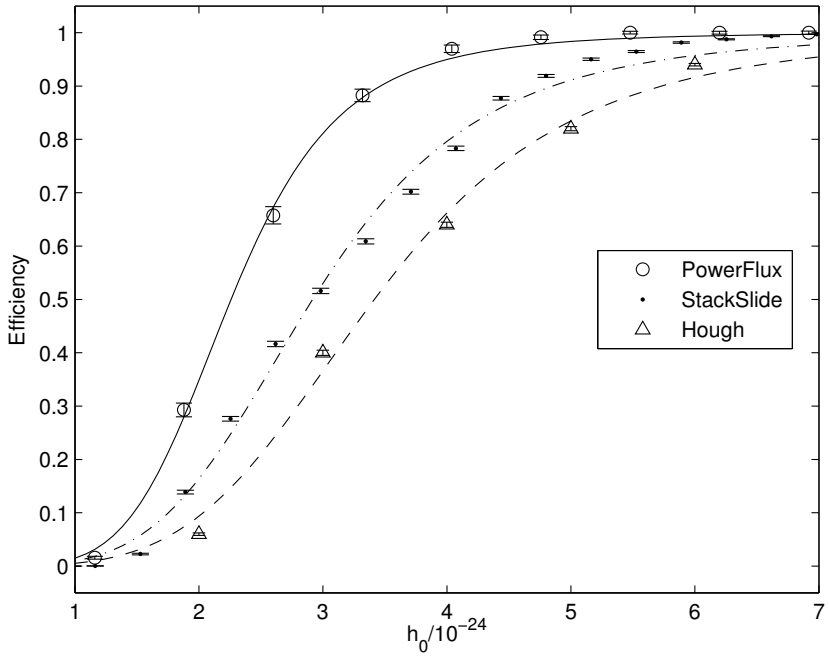

Figure 4.10: Comparison of efficiency between Hough, StackSlide and PowerFlux

In addition, injection runs were used to compare PowerFlux to Hough and StackSlide semi-coherent algorithms (figure 4.10, also see [9]). It was found that PowerFlux has the highest efficiency in well-behaved frequency bands among these three

algorithms, while Hough and StackSlide have better efficiency in highly disturbed frequency bands.

4.4 S4 run results

The detailed exposition of the first published PowerFlux results is in the S4 all-sky pulsar search paper [9]; here we will provide a summary. The search covered the 50-1000 Hz frequency band and spindowns ($\frac{df}{dt}$) between 0 and -10^{-8} Hz s^{-1}.

LIGO's fourth science run lasted approximately one month. As this is a small fraction of the Earth's orbit around the sun, the Earth's orbital velocity vector was almost stationary, leading to a large correlation between Doppler shifts and spindown corrections. Moreover, for sky locations orthogonal to the average Earth velocity vector, the Doppler shifts were more than 10 times smaller, resulting in high susceptibility to detector artifacts.

This susceptibility can be conveniently characterized by the following "S parameter":

$$S = s + \frac{\left(\vec{\Omega} \times \vec{v}_{avg}\right) \cdot \hat{\vec{r}}}{c} f$$

where s is the spindown being sampled, f is the frequency searched, $\vec{\Omega}$ is the Earth's angular velocity vector, $\vec{v}_{avg}$ is the average detector velocity, and $\hat{\vec{r}}$ is a unit sky position vector. Smaller values of S parameter indicate regions of parameter space more susceptible to stationary detector artifacts.

For this particular run we used the cutoff abs(S) $> S_{\text{large}} = 3.08\times10^{-9}$ Hz/s to determine areas of "good sky" (skyband 0 in figure 4.11), with the other 10 areas corresponding to S values from 0 to S_{large}. An example of sky partitioning is shown in figure 4.11. The 10 skybands allowed fine tuning of the actual cutoff after the production run is complete. And indeed, in the case of H1 the reported data include

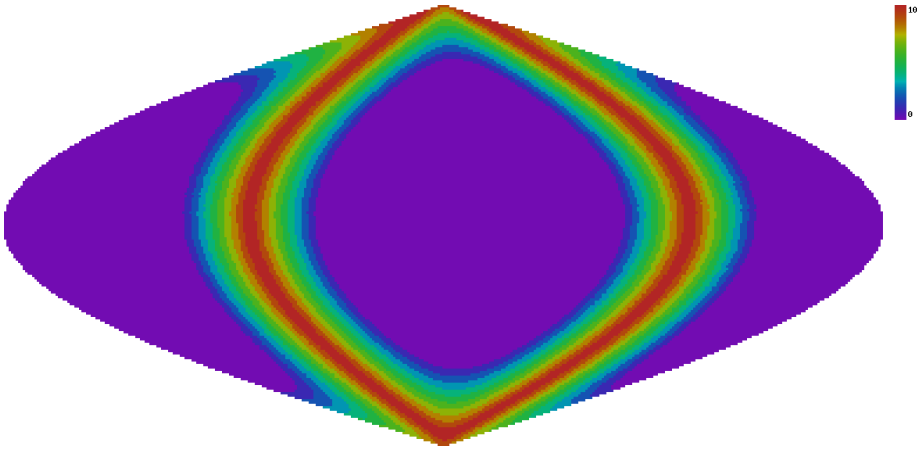

Figure 4.11: Example sky partitioning during S4 run using S parameter. Higher numbered bands indicate areas more susceptible to stationary detector artifacts.

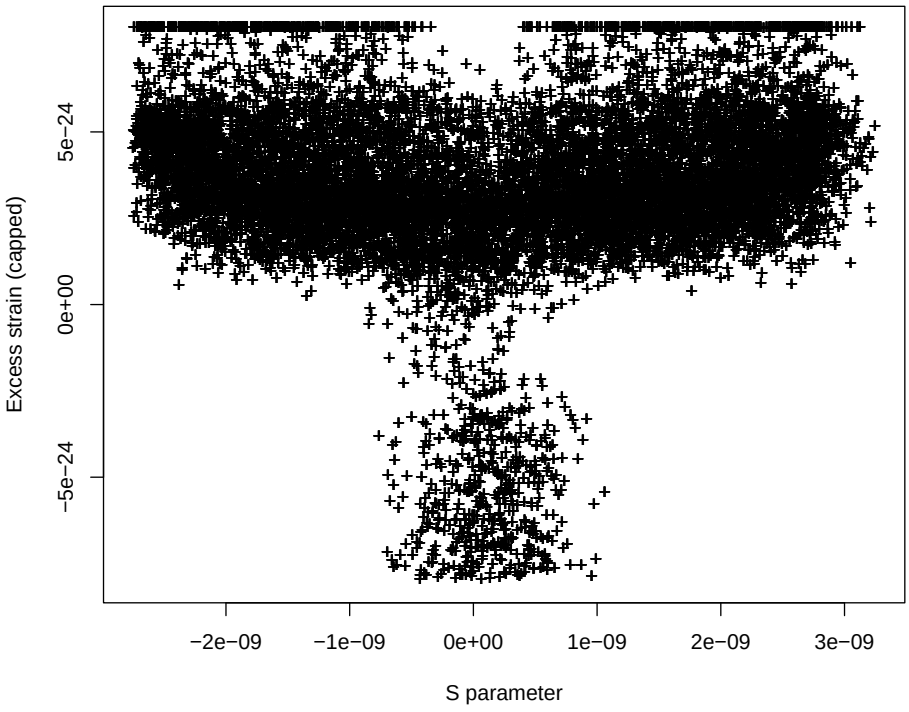

Figure 4.12: Influence of the S parameter in $140.50 - 140.75$ Hz band of H1 data. The vertical axis shows difference between the upper limit and the injected strain value.

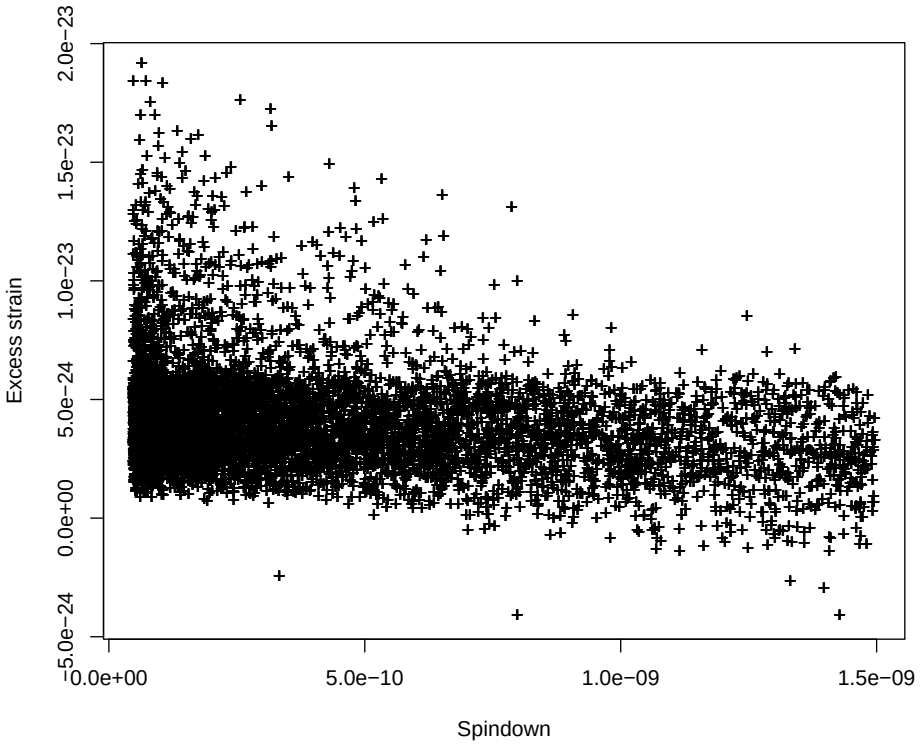

Figure 4.13: Influence of spindown mismatch in $140.50 - 140.75$ Hz band of H1 data. The vertical axis shows difference between the upper limit and the injected strain value. The horizontal axis shows injected strain value, the demodulation was performed assuming 0 spindown.

skybands 0 through 4 (corresponding to cutoff of 1.848×10^{-9} Hz/s), while L1 data includes skyband 0 alone due to larger influence of detector artifacts. The values chosen are generally conservative, as seen from the Monte-Carlo run for H1 (figure 4.12), where the "excess strain" (derived upper limit minus true value) is safely positive for large $|S|$.

The spindown stepping for high frequency bands was chosen to be 10^{-9} Hz/s which is quite conservative as seen in figure 4.13 (similar plots were obtained for injections in 550-600 Hz region). As the plot shows we could have used the same spindown stepping for all bands, except that at low frequency the partitioning of sky into bands would change too rapidly with such large spindown values. Therefore, a five times finer spindown stepping was used in the 50-200 Hz band.

A sample plot in figure 4.14 shows the most sensitive region of interferometer frequency space. The points have been color coded to reflect different noise environments encountered by PowerFlux.

The background noise level is shown in arbitrary units as a pale pink curve. We would generally expect the upper limits to conform to its shape. The green curve shows established upper limits with no anomalies.

Pale cyan dots correspond to 60-Hz regions which show contamination from power lines.

Blue dots show bands where the Kolmogorov-Smirnov test exceeded 0.07. This is indicative of distorted, non-Gaussian backgrounds, and we do not claim any limits in the affected bands.

Red diamonds mark bands where a wandering line has been detected. By itself this does not invalidate upper limits, but usually does lead to elevated numbers. The two clusters of red diamonds at 108 and 193 Hz correspond to hardware injected

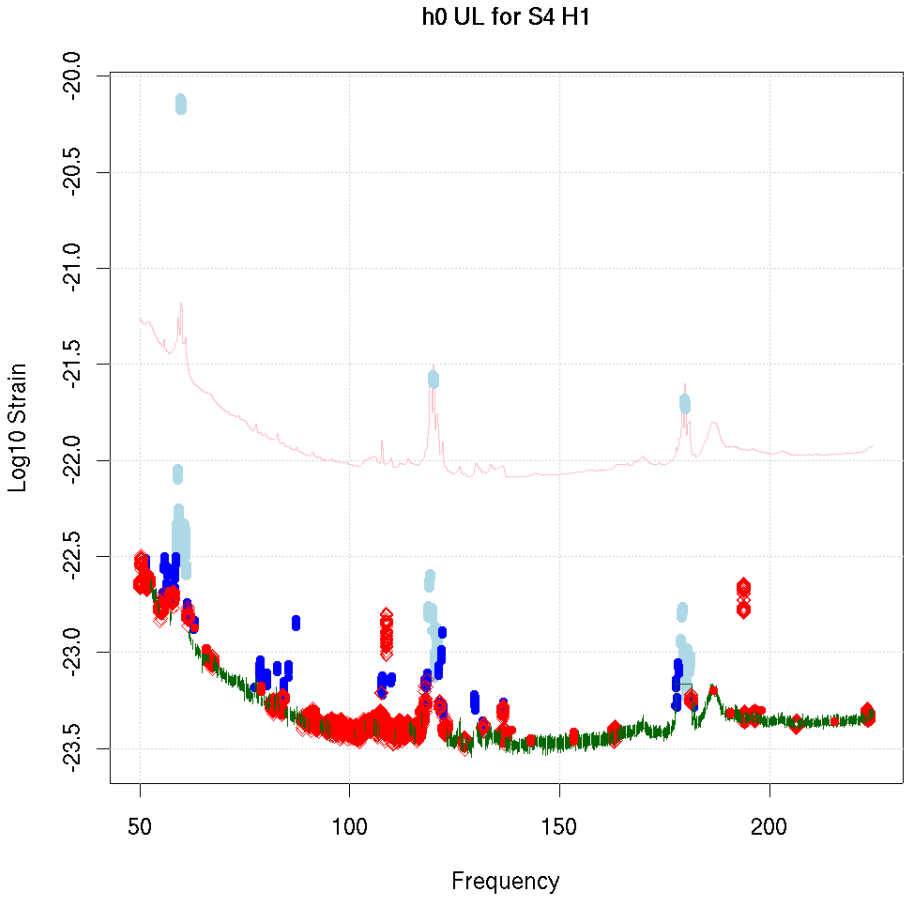

Figure 4.14: S4 H1 results in the most sensitive region of frequency space, strain

simulated pulsar signals. These were quite strong, leading to their misclassification as a wandering line.

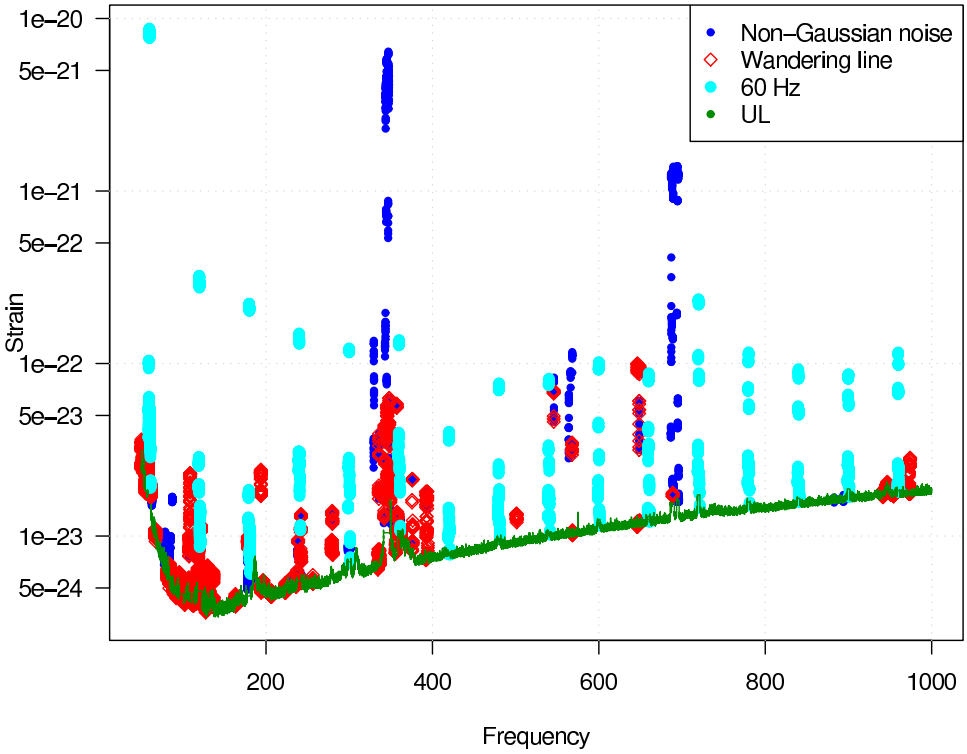

Figure 4.15: S4 H1 results, strain

Figures 4.15 and 4.16 shows upper limits for the entire searched spectrum.

4.5 Early S5 results

The entire S5 run lasted nearly 2 years, accumulating more than 1 year of triple coincidence time among the three LIGO interferometers. As of this moment, the analysis of first 9 months of S5 is complete ([10]). Since this run had a much longer time base (the interval between first and last pieces of data) the Doppler shifts exhibited a larger variation, resulting in a more uniform distribution of upper limits over the sky and better localization of potential signals (see figures 4.17 and 4.18).

Thus, instead of using S parameter which relies on large average Doppler shift,

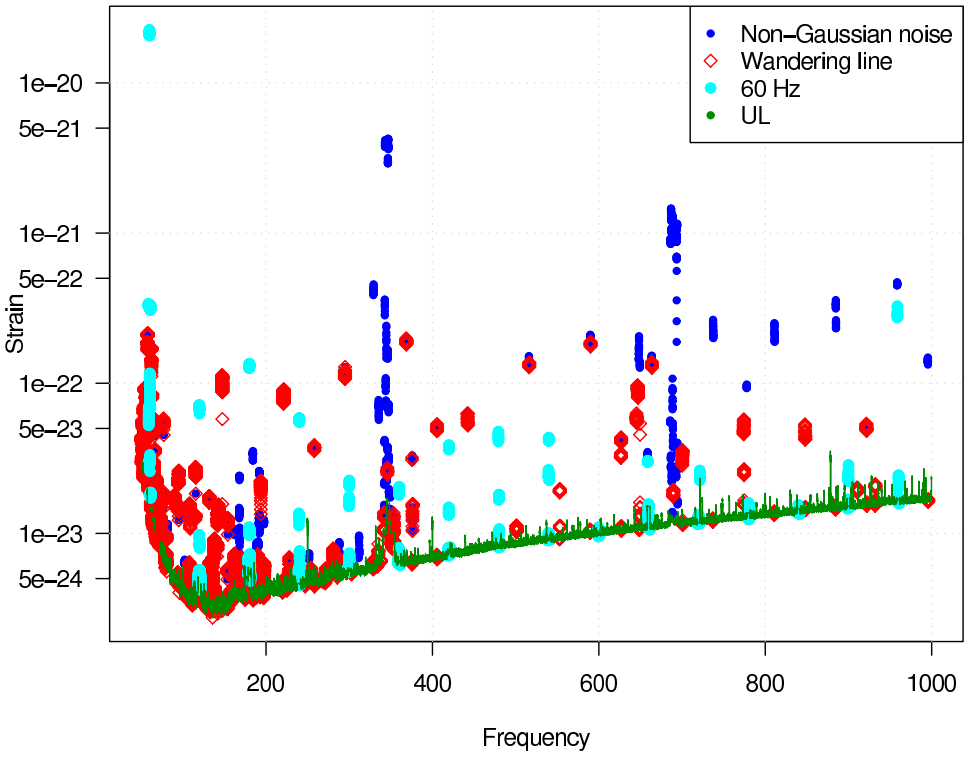

Figure 4.16: S4 L1 results, strain

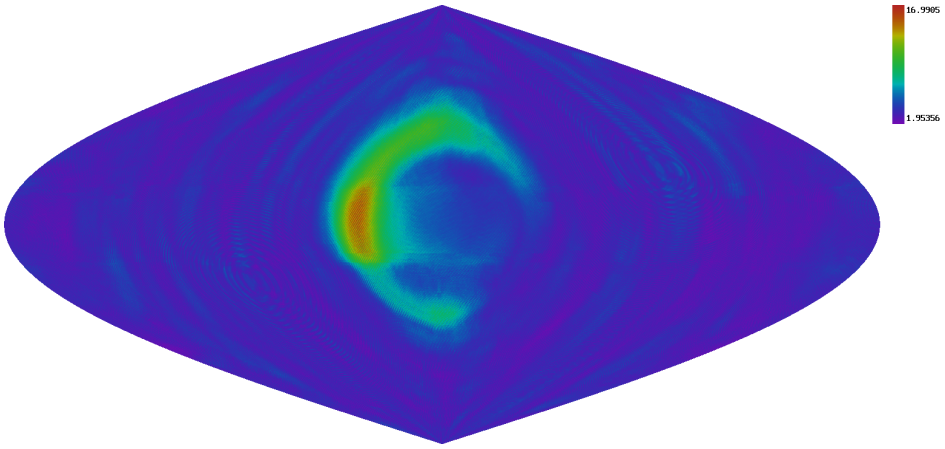

Figure 4.17: Signal to noise ratio of cross polarization for injected signal 2 during S4 run

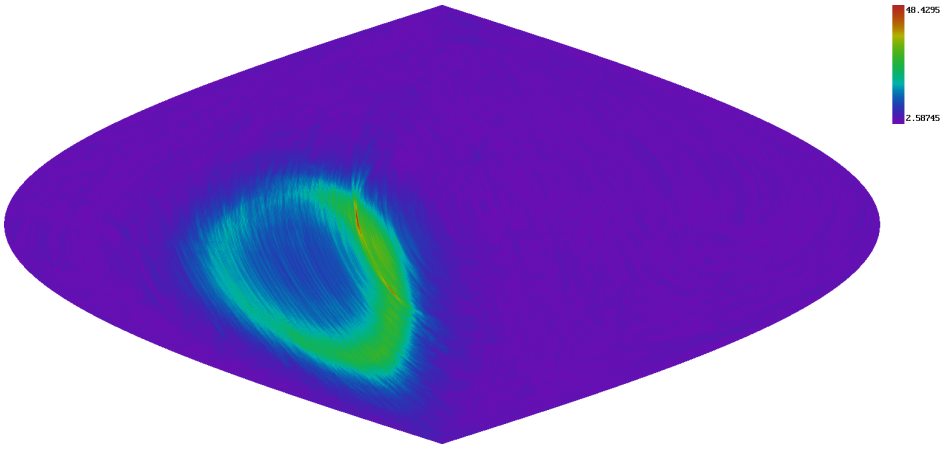

Figure 4.18: Signal to noise ratio for injected signal 2 during S5 run

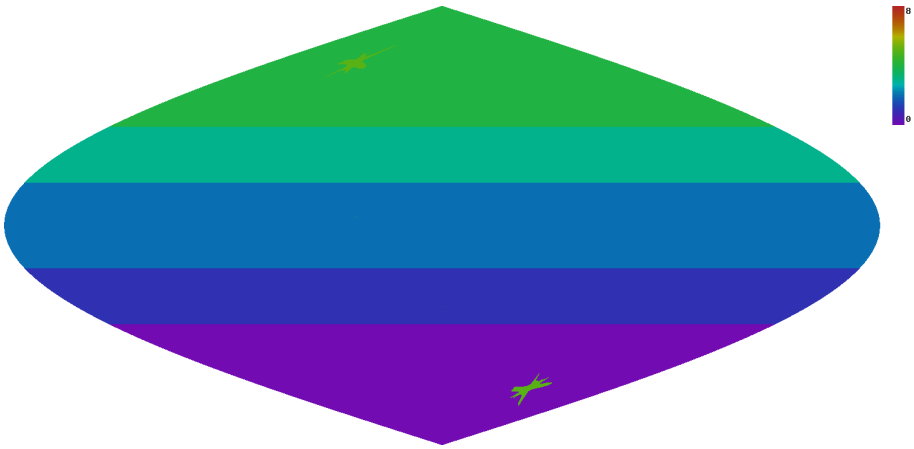

Figure 4.19: Sky partitioning during S5. The two small odd shaped regions near the ecliptic poles contain points susceptible to stationary detector artifacts

it made sense to separate the sky into 4 portions (figure 4.19): the equatorial band (with worst upper limits, red curves, see figure 4.20), the polar caps (with best upper limits, blue curves), the intermediate bands (green curves) and the region strongly affected by stationary instrumental artifacts (not shown). The upper limit curves for valid data (excluding 60 Hz lines, regions of non-Gaussianity and regions affected by instrumental artifacts) are shown in figure 4.20. We note that at smaller frequencies and for spindown values close to zero the instrumental artifacts affected a significant portion (sometimes all) of the sky, see figure 4.21.

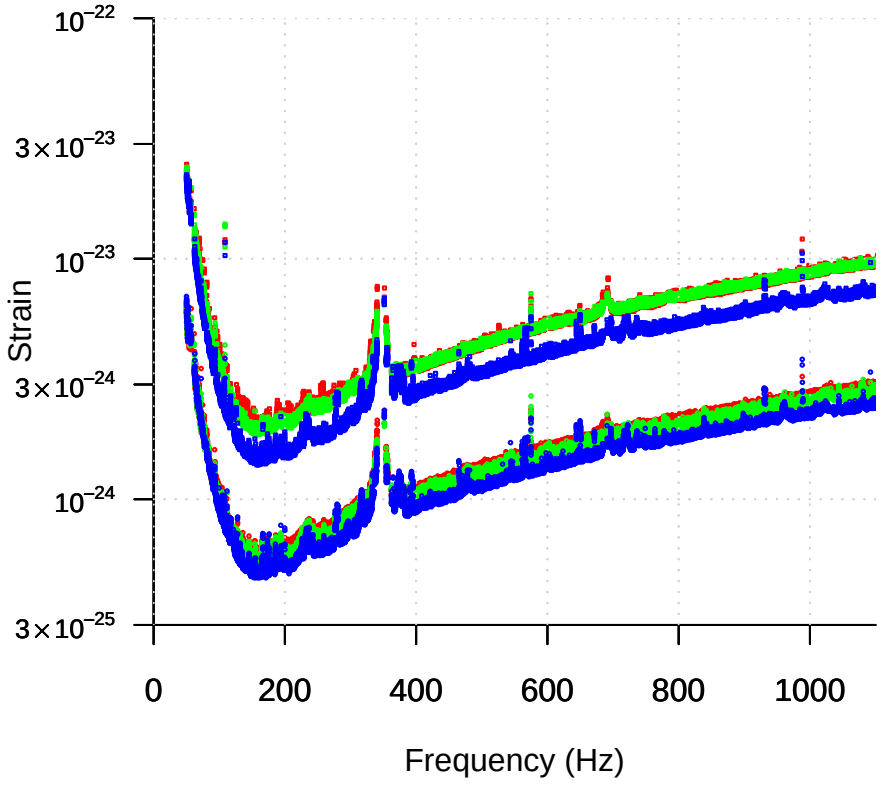

Figure 4.20: Early S5 results, strain

In addition to establishing upper limits we performed an opportunistic detection

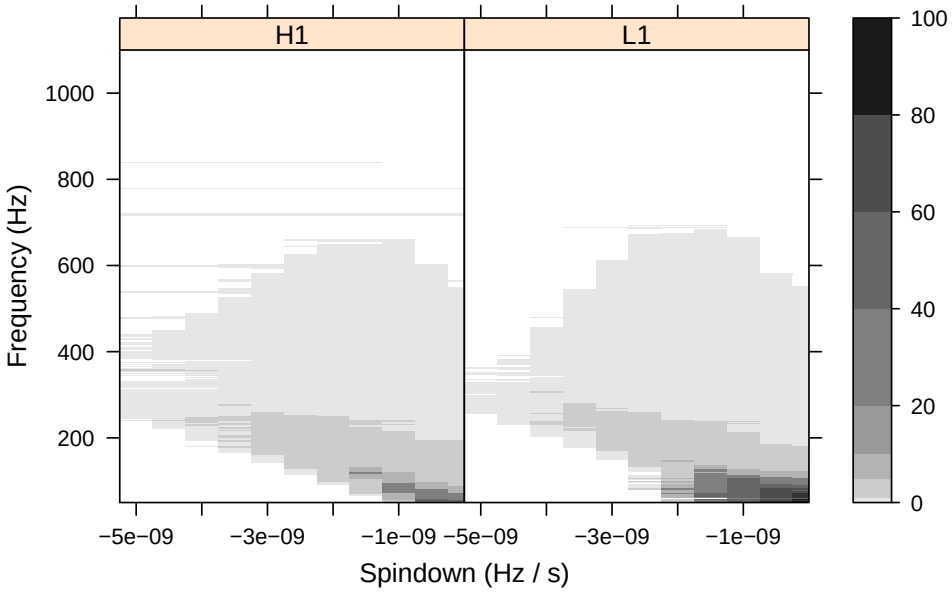

Figure 4.21: Excluded sky area (percent) in early S5 results

search by analyzing coincidences between local signal-to-noise ratio outliers of H1 and L1 interferometers.

For coincidence we required that the H1 and L1 candidates each have an SNR value greater than 6.25, their frequency difference be less than 10/1800 Hz, their spindowns be less than 4×10^{-10} Hz s^{-1} apart and their sky templates lie within 0.14 radians of each other. These parameter values have been chosen after extensive testing with simulated pulsar injections.

Most of our coincidences were due to more or less easily identifiable detector artifacts (table 4.1), in fact the particular SNR cutoffs were chosen in order to limit the number of candidates to follow up while still reaching the interesting area of coincidences with no identifiable cause, which are listed in table 4.2. Those were subjected to more intensive scrutiny, including analysis with additional data from S5 run. The conclusion was that they do not constitute a detection, as analysis using combined H1 and L1 data does not show the expected SNR increase. Nor do we see

Frequency (Hz)	Spindown (Hz s^{-1})	H1 SNR	L1 SNR	Source
89.9	1.0×10^{-10}	9.96	6.35	Electromagnetic interference
90.0	1.0×10^{-10}	9.96	6.35	Data acquisition clocking artifact
353.7	-4.0×10^{-9}	6.81	6.72	Electromagnetic interference
548.3	-4.3×10^{-9}	6.35	6.28	Electromagnetic interference
645.6	-1.9×10^{-9}	7.07	9.85	Likely L1 MC violin mode
649.6	-6.0×10^{-10}	6.45	7.11	Unknown, but seen in auxiliary channels
671.2	-4.1×10^{-9}	6.32	6.64	Likely H1 & L1 RM 2nd violin harmonics
941.1	-2.0×10^{-9}	6.50	6.67	Unknown L1 line
1006.6	-4.5×10^{-9}	6.28	6.98	Unknown L1 line

Table 4.1: List of coincidence candidates for which manual inspection immediately revealed an explanatory detector or environmental artifact. Violin modes and 60 Hz harmonics have been excluded from this list, along with artifacts due to hardware-injected pulsars.

Frequency band (Hz)	Spin-down (Hz s^{-1})	H1 SNR	L1 SNR
867.2	-4.3×10^{-9}	6.27	6.30
941.0	-2.0×10^{-9}	6.50	6.67
967.8	-1.5×10^{-9}	6.26	6.33
979.5	-5.0×10^{-9}	6.40	6.29
1058.6	-5.0×10^{-10}	6.83	6.38
1070.2	-3.0×10^{-10}	6.72	6.99

Table 4.2: List of coincidence candidates for which no instrumental spectral artifacts were observed.

an increase in SNR with longer integration times.

In particular, Monte-Carlo runs show that if we start with a coincidence that has SNR > 5.5, then the signal-to-noise ratio of a run that combines the data from both interferometers should show an increase by 2 units in at least 90% of the cases (see figure 4.22) and none of the unidentified coincidences pass this test. In addition, the studies using software injections above 850 Hz show that coincidence criteria can be tightened to 1 mHz in frequency and 0.02 radians in sky location with only a small loss of efficiency, and none of the above candidates pass these tighter constraints.

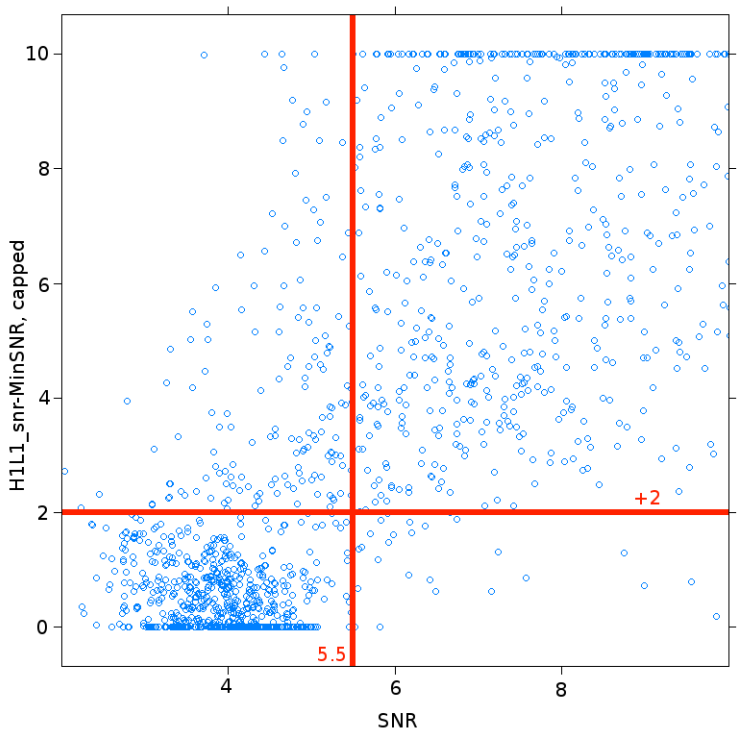

Figure 4.22: Results of injection run showing SNR improvement from combining data from two interferometers

4.6 Sensitivity, performance and future searches

The early S5 results presented above are the most sensitive blind search results to date. They are expected to be superseded by full S5 results from PowerFlux and Einstein@Home .

PowerFlux sensitivity scales as fourth root of the number of averaged SFTs and square root of coherence time.

While, theoretically, searches with longer coherence times should be more sensitive than a semi-coherent search, in practice the sensitivity is more than a matter of longer integration time. Indeed, considerations such as researcher time and availability of new and better data play an important role. In particular, the influence of detector artifacts is often only visible when the entire frequency range is covered and finding the optimal way to deal with them can require multiple iterations and many injection runs.

In addition, shorter coherence times have an immunity to a small perturbation of incoming signal, such as would be caused by a gas giant orbiting close to a neutron star or glitches due to relaxation of neutron star crust.

PowerFlux computational speed depends largely on the magnitude of Doppler shifts which dictate both sky resolution and coherence length. Because of this dependence the time to process a single 0.25 Hz frequency band grows as the square of the frequency. It is therefore tempting to increase the coherence interval at low frequencies. Doubling this interval will increase the sensitivity by 19% and, more importantly, improve resiliency to detector artifacts.

The last goal is of particular importance, as the study of high SNR outliers is limited by how many coincidences we can investigate in detail. Dealing with detector

artifacts thus directly (and greatly) improves sensitivity of detection search.

The full-S5 search is now in progress. It has two major changes from the early S5 results described above. First, the upper limits code has been rewritten to be more modular and to better handle closely spaced spindowns and Doppler shifts. It has shown an increase in computation speed by a factor of 10 at high frequencies. Secondly, instead of searching for high-SNR outliers in H1 and L1 data separately, the search is performed on H1, L1 and combined H1-L1 data simultaneously, and the high-SNR threshold is established on the combined H1-L1 data, which is then used to find close H1 and L1 outliers with SNR > 5 (as compared with the SNR > 6.25 condition used in early S5 search).

LIGO's sixth science run has just started acquiring data, and we expect to have data with 2 times better sensitivity at high frequencies and improved prospects for a detection. For this analysis it is planned to improve PowerFlux with a capability to coherently combine simultaneous SFTs from different interferometers.

CHAPTER V

Wavefront camera

As the laser beam is a core component of the interferometer, one needs to monitor its quality and to understand its behaviour. A wavefront camera is a device for observing the cross section of the laser beam at RF frequencies.

Such a device can be employed for observing sideband shape, monitoring thermal effects on interferometer optics and as a diagnostic for misalignment.

As with oscilloscopes, there are many different approaches - one can sample the beam one pixel at a time and scan across the cross section, one can make short exposure images and one can digitize multiple pixels at high speeds. For our design we have chosen the last because of its flexibility and lack of assumptions about laser beam behaviour and because of better scalability.

As the LIGO interferometers modulate laser beams at 20-40 MHz we wanted a prototype capable at sampling at 100 MHz at least four channels, with an eye towards building a camera with hundreds, if not thousands, of channels. This necessitated great attention to per-channel costs.

The camera naturally splits into four subsystems:

- Computer interface/data readout unit
- Analog to digital conversion unit

- Sensor unit
- Light sampling optics

5.1 Computer interface/data readout unit

This part of the system should acquire the data, buffer it and transmit to a regular computer for analysis. The smallest reasonable resolution of analog to digital converters is 8 bits, which implies a data acquisition rate of 100 MB/sec, 400 MB/sec for four channels. This presents severe constraints both in terms of board electronics and computer interface.

At the moment there are few commodity high speed interfaces available for such a project:

- USB - version 2.0 can reach speeds as high as 30 MB/sec. This is marginally sufficient for near real time observation, provided some data reduction technique (like band pass) is employed. True real time transfers over USB require isochronous mode, which has a substantially smaller bandwidth. There are multiple interface chips on the market, including a very convenient CY7C68013 from Cypress Semiconductor.
- SATA - currently available interfaces can reach speeds of 100 MB/sec or more, but implementation is hampered by the lack of a convenient interface chip. One could deploy an FGPA for such purpose, but it would have to be capable of high speed serial link (at least 1.5 Gb/sec). Low cost FPGAs with such capabilities are just starting to appear and might present an interesting opportunity for new design. In particular, it might be possible to use a high-end RAID array card as a way to deliver data from multiple boards.

- Ethernet - 1Gb/sec is capable of delivering 80-90 MB/sec streams, and a 10 Gb/sec variant should be able to carry real time data of eight channels. There are many interface chips available on the market, but they are either specific to computer networking applications or accept data via interfaces not easily accessible by low-cost FPGAs.

- PCI/PCI Express - a regular 32 bit PCI bus can handle 100 MB/sec stream, but this would likely put a lot of strain on the computer I/O subsystem. The newer PCI Express bus can handle a much larger bandwidth with GB/sec utilized by computer graphics hardware. PCI Express is a serial interface and thus requires more expensive FPGAs. In addition typical computer mainboards have only a few high speed channels, limiting the number of devices one can connect.

Out of all these possibilities we strongly prefer Ethernet due to strong commercial and public support - there are many low-cost switches and interface cards, along with example code and documentation. There are also advantages of easy integration with existing computing clusters and the ability to separate data collection from processing equipment (which, for example, would have a benefit of eliminating computer fan noise).

Our ideal board would have a gigabit PHY chip, an FPGA dedicated to network control and a data acquisition and processing FPGA with user uploadable bitstream and at least 32 high speed input/output pins dedicated for data exchange with external device.

Unfortunately, there is no practical commercial device that meets this description. There are many boards with a 100 Mbit interface which is too slow for our purpose. There are boards with gigabit PHYs and high-end FPGAs, but they are very expensive due to the FPGA cost and also because of closed-source software necessary to

program the FPGA.

It should be possible to produce a custom board. This allows better control of FPGA pin utilization and more flexibility. The disadvantage is the larger development time and increased cost. In addition, larger FPGAs are produced only in BGA packages which consist of a grid of small solder balls on the underside of the package. We are not aware of any economical way to work with such chips in small quantities. At best one can opt to use a hot air iron or an oven, but this would exclude any way of correcting attachment errors. A socket is possible, but they often cost as much or more than the actual chip.

Thus after review of many alternatives we have settled on using the Nexys board produced by Digilent. This board has a 40-pin high speed connector, USB 2.0 interface using CY7C68013 chip (which, unfortunately, was connected in such a way as to cut available bandwidth in half) and a Xilinx Spartan FPGA. Our version with a 120M gate FPGA was priced at $120. For comparison, the same FPGA chip is $60 in single quantities, and it costs around $200 to produce a custom four-layer printed circuit board.

5.2 Analog to digital conversion board

It is possible to purchase a commercial digitizer board. While many of these boards have very good specifications, most have smaller sampling rates (below 60 MHz) which is possibly an artifact of PCI bus transfer speeds. High-speed boards typically cost at least $1000 per channel, and we are not aware of any PCI or PCI Express board with four fast analog channels.

Therefore we have constructed our own board. Each channel consists of one Analog Devices analog to digital converter AD9283 and one amplifier AD8369. The

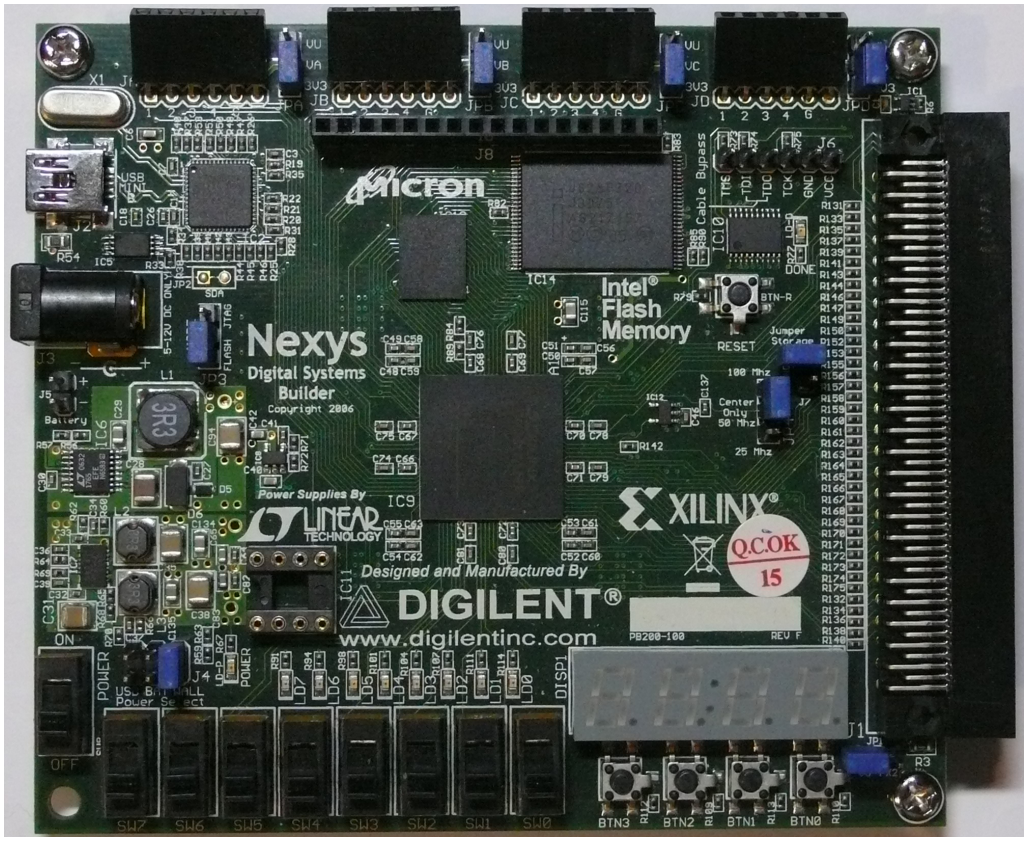

Figure 5.1: Nexys board by Digilent, Inc.

latter is a variable gain amplifier with digital gain control.

In addition, there are two PCA9539D expander chips that set the gain on the amplifiers, control power down mode and a few diagnostic LEDs.

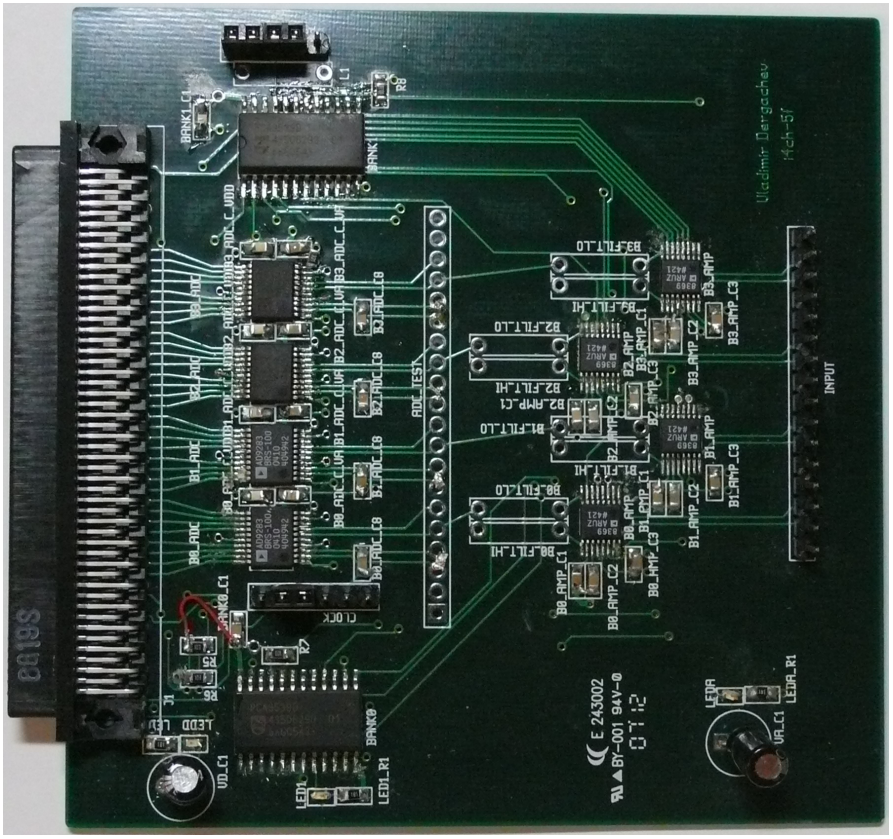

Figure 5.2: Analog to digital converter board

5.3 Sensor unit

One of the less trivial aspects of designing the camera is the choice of sensor for conversion of light intensity into electrical signal. We provide a brief overview of available devices:

- CCD/CMOS sensors - in theory, these sensors could provide the necessary speed and accuracy. However, all currently available devices are designed for relatively slow exposure times and readout. This is not too surprising if one considers that

an 8x8 matrix sampled at 100 MHz produces a stream of 6.4 GB/s. A chip capable of safely transmitting that much data requires very careful design, while the relatively small resolution limits possible applications. A larger 256x256 matrix would result in 65 TB/s stream presenting an enticing engineering challenge. It is possible to achieve small exposure times by using a microchannel plate, but this provides only a single frame.

- PIN photodiodes - these are the conventional RF sensing devices. Many models are available in a reasonable price range. One big issue is that photodiodes produce current, not voltage, which needs to be converted by a transimpedance amplifier (TIA). Barring exotic sensing schemes [25], a transimpedance amplifier acts as if we discharged our photodiode through a sufficiently large resistor. The bandwidth then becomes dependent on the RC product of the sensing resistance and the internal capacitance of the photodiode. To reduce capacitance a typical low-cost high-speed photodiode has a very small sensing area, on the order of 0.25mm^2.

- PIN/TIA modules - these are relatively new devices consisting of a PIN photodiode and transimpedance amplifier in a single package. They are manufactured in large quantities for optical networking hardware. There are commercial modules with bandwidth as high as 10 GHz. Most come equipped with specialized connectors that mate to single-mode or multi-mode fibers.

- Avalanche photodiodes - these operate at fairly large reverse voltage and combine high amplification with fast response. They are commonly used in high speed data links. At the moment we are not aware of any low cost models available in small quantities.

- Photomultipliers - most models have 10ns or slower response. Conventional models have difficulties correlating light intensity and output current (as they were made to count single photons).

- Photoresistors - these are fairly slow devices with millisecond response times.

At this point only PIN photodiodes or PIN/TIA modules would allow a large channel count at a reasonable cost. We have explored three different possibilities:

- Plain OP906 photodiodes (made by Optek, Inc.) operated in a photovoltaic mode. These were discharged into a 50 Ohm impedance which should allow for at least 150 MHz bandwidth. The plastic lens obviates the need for a separate optics frontend (see figure 5.3) which would make alignment easy. The drawback is the expected poor sensitivity and susceptibility to noise.

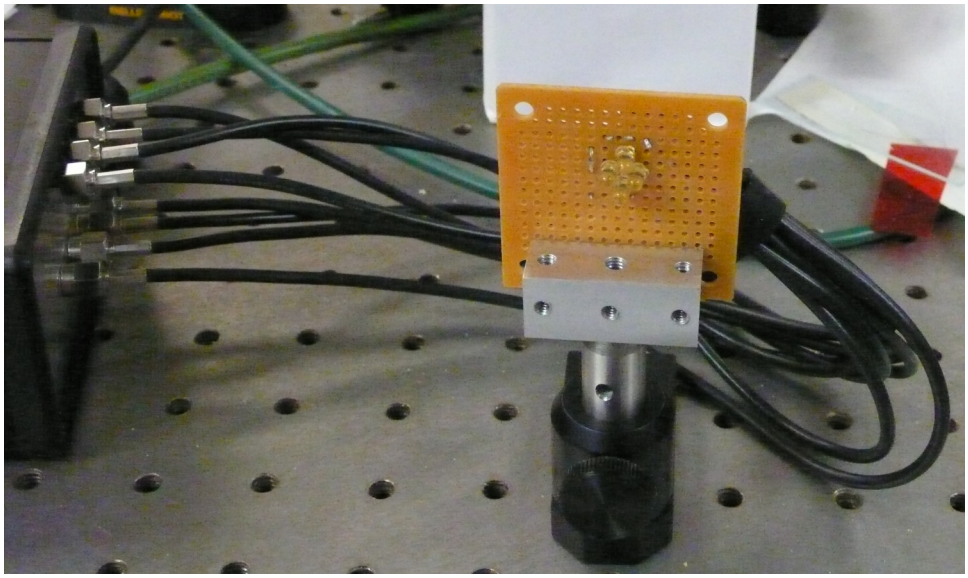

Figure 5.3: Sensor frontend built with OP906 photodiodes

- OPF2416 PIN/TIA modules (also, by Optek, Inc., figure 5.4). These modules have a standard ST connector that accepts a multimode fiber optic cable with core diameter as large as 100 um and they are rated for a 125 MHz bandwidth.

Complete frontend board is shown on figure 5.5.

Figure 5.4: Photodiode module OPF2416T by Optek, Inc.

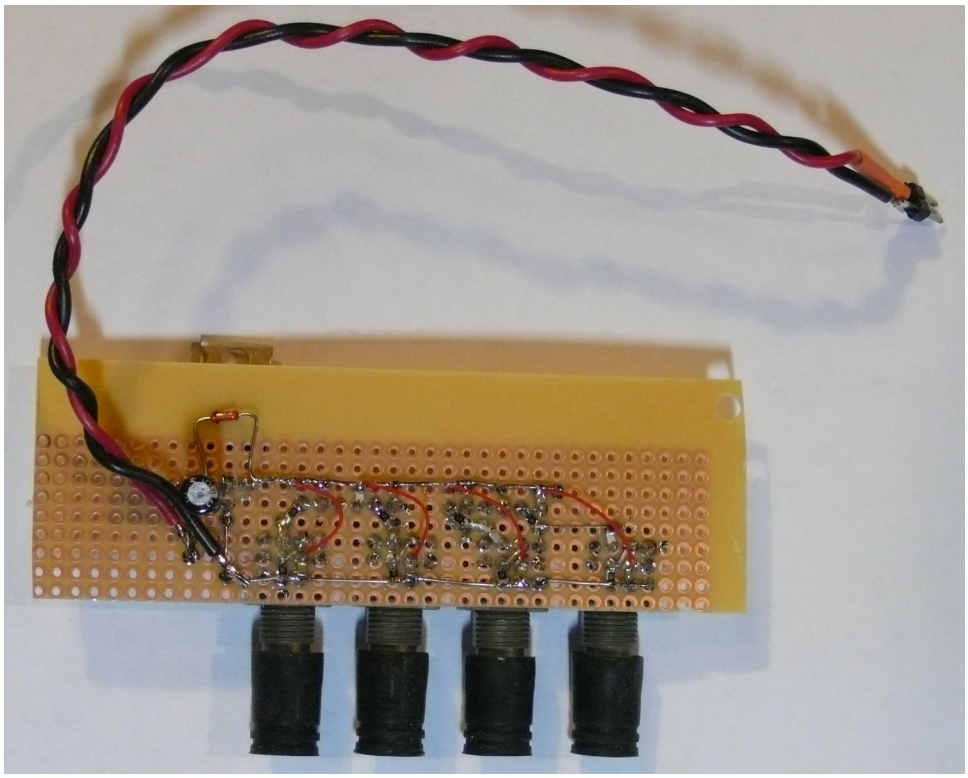

Figure 5.5: Sensor frontend board built with OPF2416T modules

- PL-SLR-00-S23-C1 PIN/TIA modules (by JDS Uniphase, figure 5.6) with 2.5 GHz bandwidth. These modules come with a connector that accepts a 1.25 mm ferrule, such as found in SC fiber optic connectors. In application, these plastic connectors were removed exposing a small ball lens. The modules were integrated with the optics unit and connected to the analog to digital converters

via differential 50 Ohm cables (see figure 5.7).

Figure 5.6: PL-SLR-00-S23-C1 module

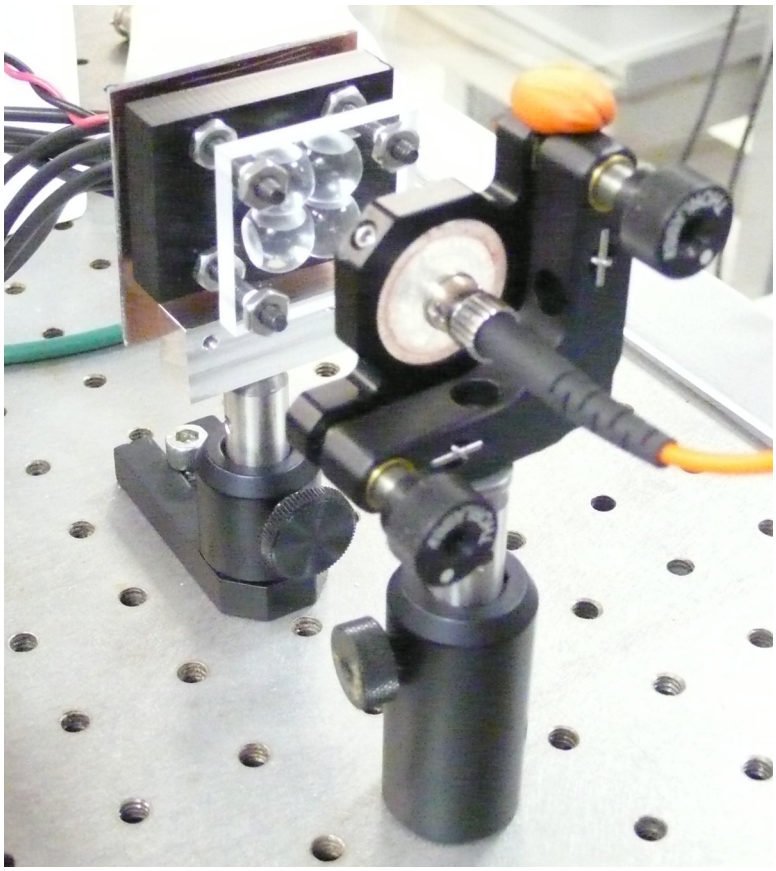

Figure 5.7: Sensor frontend board built with PL-SLR-00-S23-C1 modules

5.4 Firmware and software

There are several programmable components of the design (5.8). The prototype host data acquisition program was written in Python mostly due to the ease of making plots and accessing the USB bus. The firmware for the USB controller was

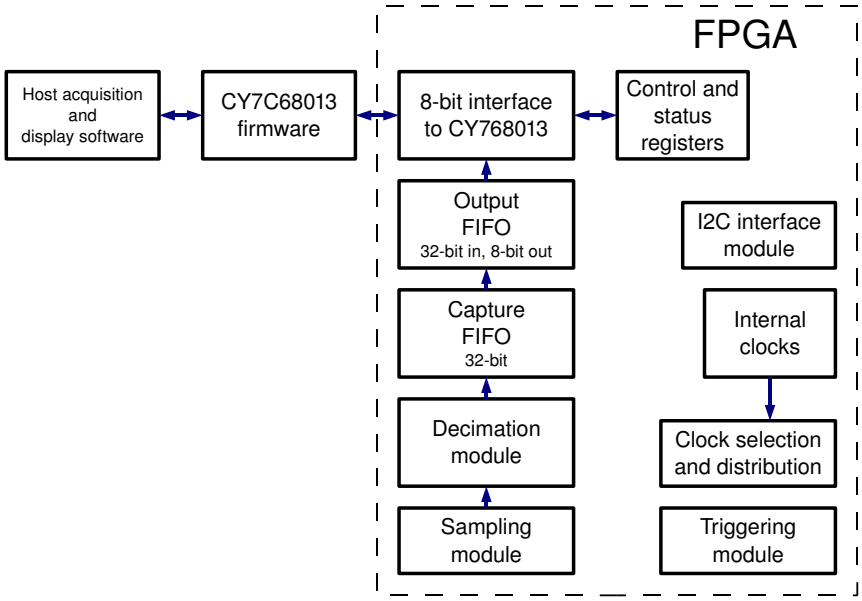

Figure 5.8: Firmware and software architecture

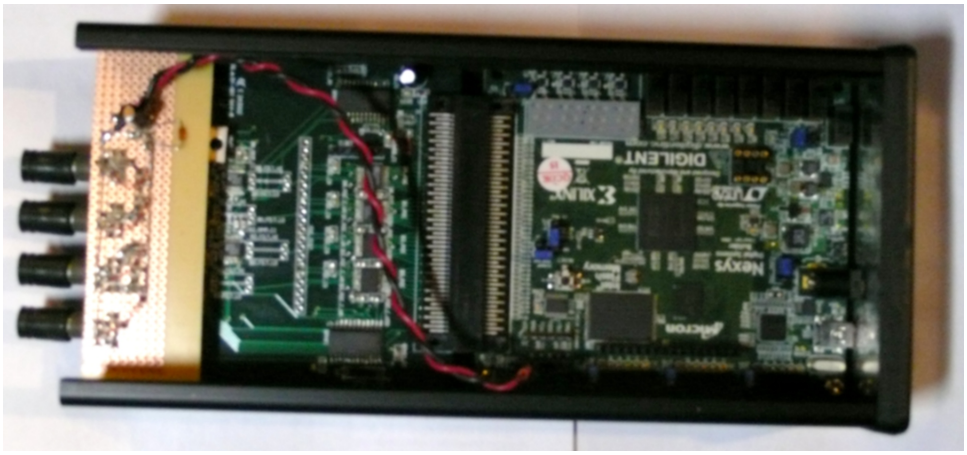

Figure 5.9: Electronics box, shown with frontend based on OPF2416T modules

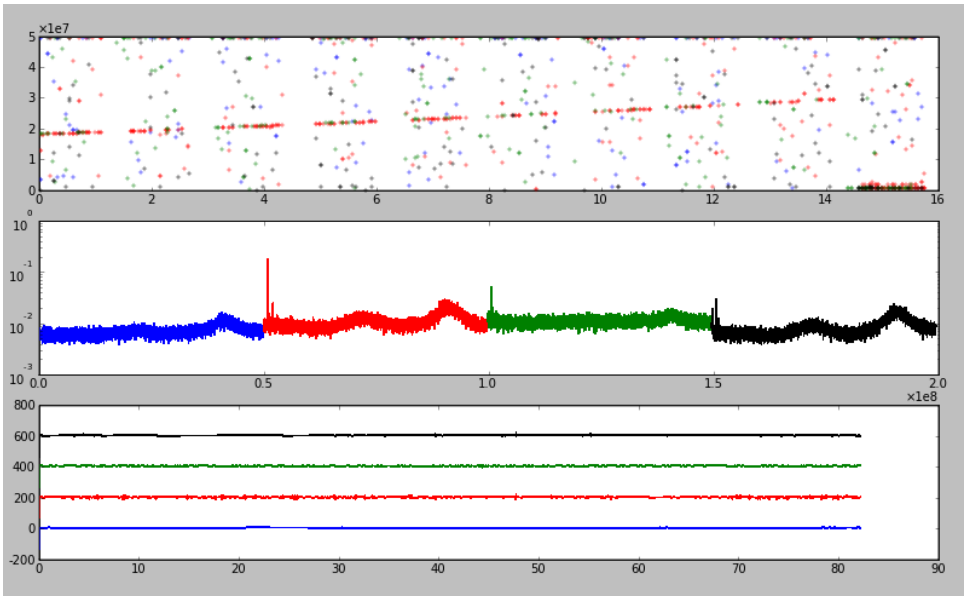

Figure 5.10: A display snapshot during $1 - 30$ MHz frequency sweep of PL-SLR-00-S23-C1 based frontend. The upper plot shows frequency increasing from 20 to 30 MHz, after which the sweep resets. The middle plot shows averaged power spectrum for the last data acquisition stretch. The bottom plot shows data for the last captured waveform. The beam was off center, focused on channel 1, see also figure 5.14

written in C and compiled with the SDCC ([17]) compiler.

The most complicated piece was the firmware for the FPGA. While conceptually simple, the 100 MHz operating speed is right at the border of what is possible for this chip, and careful attention needed to be paid to clocks and data paths. The firmware was implemented in Verilog using Xilinx Webkit. The FIFOs were generated by special purpose Xilinx tools in order to best use available hardware resources. We have also borrowed the I2C controller module from OpenCores project([18]).

The assembled electronics box (5.9) was tested and was found to respond to several micro Watts of modulated light. Figure 5.10 shows a screenshot of the host program displaying data from a frequency sweep signal in real time. The top plot shows the evolution of high signal to noise ratio lines over time. The X axis is in seconds with gaps due to the time taken by the laptop computer to update the plot. The Y axis

is frequency. Different colors mark data from different channels, blue corresponds to channel 0, red is channel 1, green is channel 2 and black is channel 4.

The middle plot shows averaged power spectrum data with low frequencies excluded - they contain noise peaks which are likely due to coupling of digital signals via power supply lines.[1] The peaks at the signal frequency are clearly visible. Different channels respond differently, as the beam is off-center.

The bottom plot shows snapshots of time-domain data from four channels. The X axis is in 10 ns units, the Y axis are counts from analog to digital converters. For clarity, the curves have been offset by 200 units.

5.5 Input optics

While the OP906 photodiode comes with its own lens built into the packaging, both PIN/TIA modules require additional optics to guide the sections of the laser to the sensors.

A single channel device is constructed of a machined acetal plate and an acrylic ball lens, see figure 5.11. In the case of a OPF2416T module it couples to a multimode fiber, while a PL-SLR-00-S23-C1 is directly inserted into the channel after removing the plastic casing from the module. In both cases we have used a 0.5" acrylic ball, but varied the diameter of the hole and the thickness of the plate. Acetal was chosen over aluminum to prevent the fiber optic ferrule from becoming jammed in the hole.

A multiple-channel device is shown in figures 5.7 and 5.12. In both cases a transparent acrylic plate is used to retain the balls, which have been machined to a square cross section in order to better cover the illuminated area.

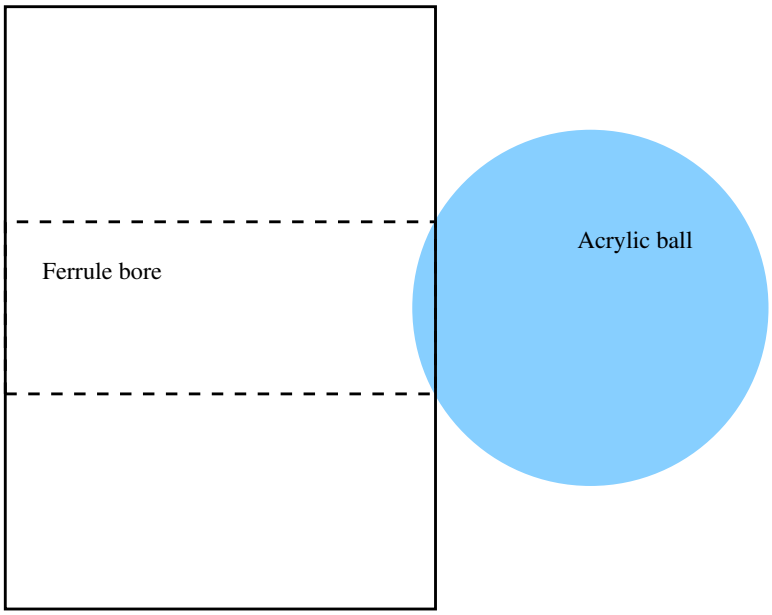

Figure 5.11: Single channel multimode fiber coupler

5.6 Testing

The testing of the wavefront camera components proceeded throughout the development cycle. First, the FPGA board, individual photodiodes and PIN/TIA modules were checked for correct operation. Next, the analog-to-digital converter board was assembled and connected to FPGA. A small error in the I2C bus connections was found and fixed. Then we assembled the sensor boards and tested each sensor individually.

Lastly, the optics frontends were developed and tested. This stage proved to be the most difficult, as we did not have access to a light source of sufficient power and modulation depth. For testing we used a homemade laser module (figure 5.13) based on a 850 nm OPV314 VCSEL laser from Optek, Inc. This provides 10-50 μW of power depending on whether it is coupled directly to the sensor or over a distance via a focusing lens.

[1] An additional source of noise is the offset compensation loop of the amplifiers, however it is configured to operate at a very low frequency.

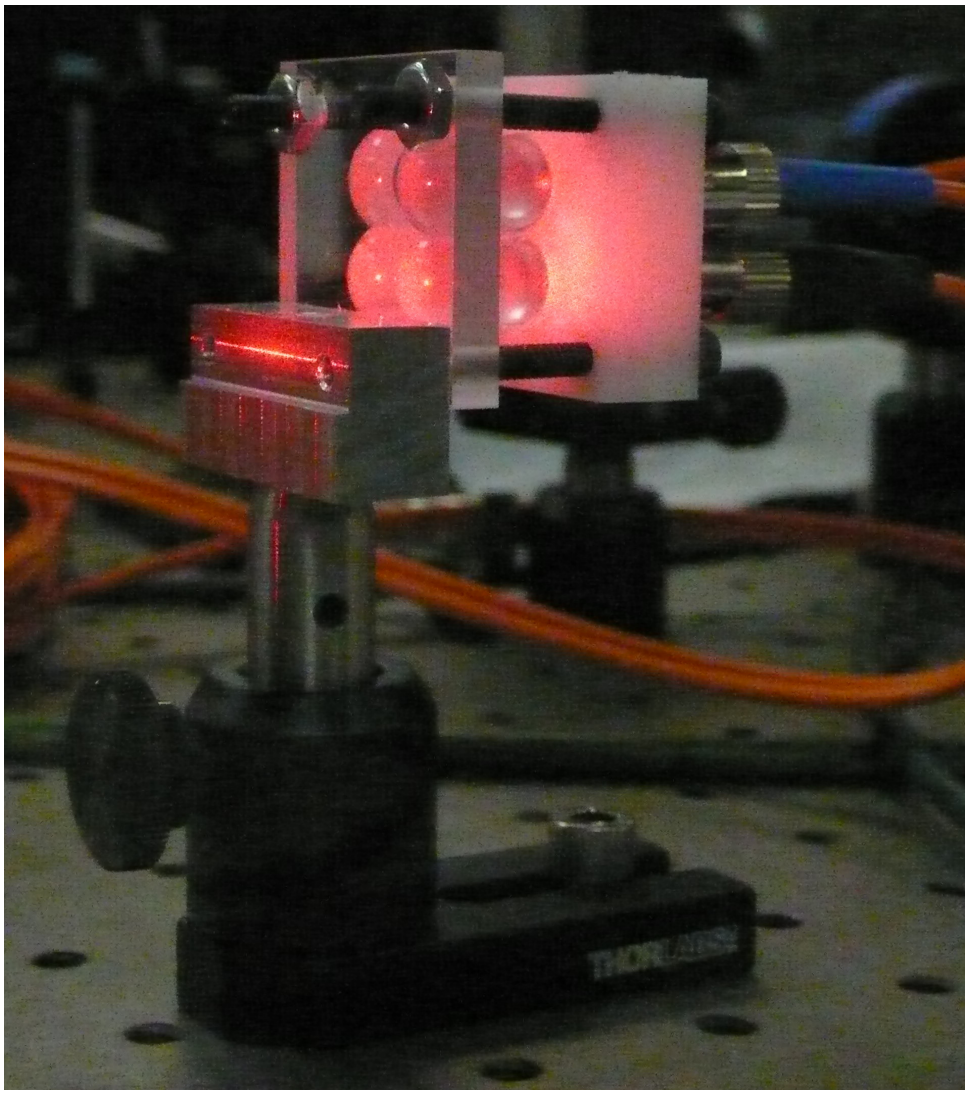

Figure 5.12: Input optics prototype

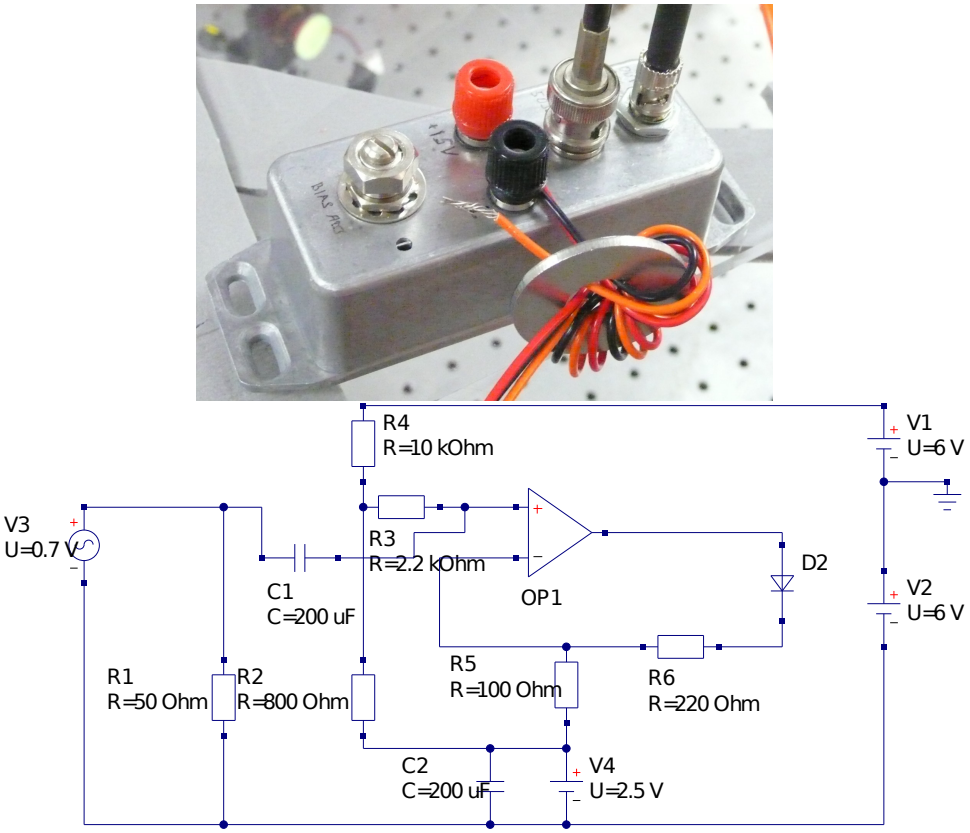

Figure 5.13: Laser diode module used in testing

The baseline design consisting of four OP906 photodiodes was easy to align and showed bandwidth extending to at least 10 MHz. However, one had to use the maximum gain settings on the amplifiers to see the signal, and testing of higher frequencies could not be done because of a rising noise floor.

The design based on the OPF2416T connected via multimode fibers was found to be unsatisfactory for two reasons.

First, less than a hundredth of the incident light was coupled into the fibers. The major cause is the small acceptance angle. Since the sampled beam has to span all the optics, only a small portion of the area is being utilized. In addition, there are strong interference effects which further degrade coupling efficiency.

Secondly, the diffraction effects make the device very sensitive to vibration - tapping the prototype produced visible variation in the light output from the fibers.

While the first issue can be mitigated with smaller lens apertures and more closely spaced fibers, the small size of the fiber core would require illumination with an incoherent beam to get rid of noise coupling which limits possible applications.

The design based on the PL-SLR-00-S23-C1 modules was more successful, producing strong signals after a moderate alignment effort (see figures 5.10 and 5.14 - they show results of a frequency sweep from 1 MHz to 30 MHz where the expanded beam was aimed on one sensor element). It has two limitations: first, the large coupling lens and the small lens built into the module produce Keplerian telescope with ≈ 9 magnification power. This made alignment much more critical than we would have preferred. Secondly, the acrylic ball lenses did not self-align sufficiently to work out of the box; some tweaking was required. This is due to friction of the retaining acrylic plate. A better design would be to machine the balls into a cylindrical shape that fits directly into the acetal plate holding the modules.

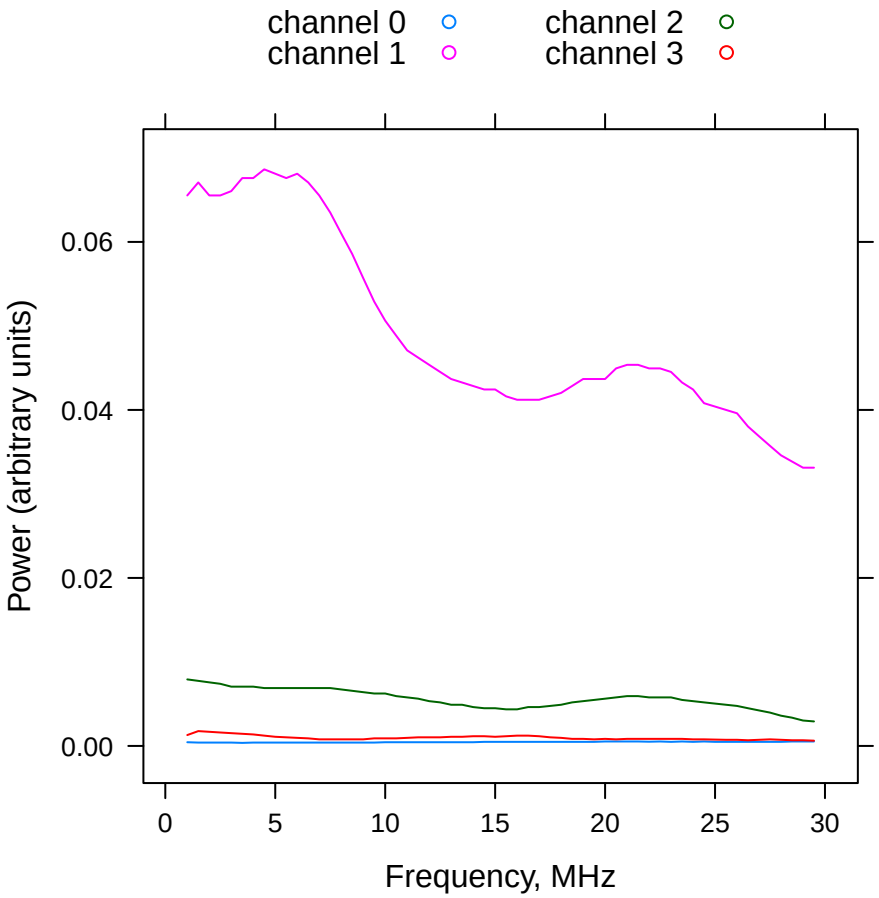

Figure 5.14: Response of PL-SLR-00-S23-C1 frontend to frequencies in the range of 1-30 MHz, beam off center and focused on channel 1, see also figure 5.10

5.7 Scalability and future directions

Our goal has been to demonstrate feasibility of building an economical direct sampled data acquisition system capable of sampling a laser beam cross section at 100 mega samples per second or faster in 10×10 channel matrix or larger. We believe this has been achieved. Specifically:

- The part cost of sensors and electronics boards is less than $350 for four channels. Thus 100 channels can be achieved for under $9000 - the price of a medium range oscilloscope. Furthermore, for some applications it is sufficient to only sample a few mixes of sensor signals at a time - this can be achieved with fewer channels and an analog mixer controlled via FPGA.

- The optics frontend can be fabricated using regular machine shop techniques. For a larger device, instead of using acrylic balls we recommend either finding a good commercial multi-lens array or fabricating our own plastic lens from a form machined with high precision CNC machine. The latter would allow to tailor the lens properties to our application.

- During testing we used 850 nm communications VCSEL laser, as opposed to 1050 nm utilized in LIGO interferometers. The coefficient of refraction for acrylic does not change appreciably over this frequency range, so the same optics design can be utilized.

CHAPTER VI

Conclusion

The search for gravitational waves is an exciting new frontier of exploration, presenting challenges of analytical, computational and technical nature.

We have presented the results of searches for continuous wave gravitational radiation with PowerFlux. At the highest frequency sampled of 1100 Hz we are sensitive to neutron stars of equatorial ellipticity 10^{-6} within 500 pc range (see [9] for formulas relating range and sensitivity). This ellipticity is below the upper range possible for conventional neutron stars (see [26]) and orders of magnitude lower than what could be sustained by a strange quark star (see [27]).

Presently only ~ 25 neutron stars emitting in radio or X-rays are known within 500 pc [28], compared to $O(10^4 - 10^5)$ electromagnetically quiet neutron stars that we expect from birth rate calculations [29], although, of course, the number accessible to LIGO [30] and remaining in this volume [31] would be much smaller. New opportunities to find electromagnetically quiet neutron stars await in the ongoing analysis of full S5 data and later science runs.

We have also described a prototype for a wavefront camera and the path to building a full instrument.

BIBLIOGRAPHY

BIBLIOGRAPHY

[1] "Measurements of General Relativistic Effects in the Binary Pulsar PSR1913+16" , J.M. 1979, Nature 277, 437

[2] First upper limits from LIGO on gravitational wave bursts, B. Abbott *et al.* (The LIGO Scientific Collaboration), Phys. Rev. D **69** 102001 (2004).

[3] Limits on Gravitational-Wave Emission from Selected Pulsars Using LIGO Data B. Abbott *et al.* (The LIGO Scientific Collaboration), M. Kramer, and A. G. Lyne, Phys. Rev. Lett. **94** 181103 (2005).

[4] Upper limits on gravitational wave emission from 78 radio pulsars B. Abbott *et al.* (The LIGO Scientific Collaboration), M. Kramer, and A. G. Lyne, Phys Rev. D **76**, 042001 (2007).

[5] Searches for periodic gravitational waves from unknown isolated sources and Scorpius X-1: Results from the second LIGO science run B. Abbott *et al.* (The LIGO Scientific Collaboration), Phys. Rev. D 76 (2007) 082001

[6] The Einstein@Home project is built upon the BOINC (Berkeley Open Infrastructure for Network Computing) architecture described at `http://boinc.berkeley.edu/`.

[7] Einstein@Home search for periodic gravitational waves in LIGO S4 data, B. Abbott *et al.* (The LIGO Scientific Collaboration), Phys. Rev. D 79, 022001 (2009)

[8] Einstein@Home search for periodic gravitational waves in early S5 LIGO data, B. Abbott *et al.* (The LIGO Scientific Collaboration), arXiv:0905.1705

[9] All-sky search for periodic gravitational waves in LIGO S4 data, B. Abbott *et al.* (The LIGO Scientific Collaboration), Phys. Rev. D **77**, 022001 (2008).

[10] All-sky LIGO Search for Periodic Gravitational Waves in the Early S5 Data, B. Abbott *et al.* (The LIGO Scientific Collaboration), Phys. Rev. Lett. 102, 111102 (2009)

[11] Bernard F.Schutz (1990). A first course in general relativity. Cambridge University Press.

[12] C. W. Misner, K. S. Thorne, and J. A. Wheeler (1973). Gravitation. W. H. Freeman and Co.

[13] Peter R.Saulson (1994). Fundamentals of interferometric gravitational wave detectors. World Scientific.

[14] Data analysis of gravitational-wave signals from spinning neutron stars. I. The signal and its detection. P. Jaranowski, A. Królak, and B. F. Schutz, Phys. Rev. D **58**, 063001 (1998).

[15] A Radio Pulsar Spinning at 716 Hz . Jason W. T. Hessels, Scott M. Ransom, Ingrid H. Stairs, Paulo C. C. Freire, Victoria M. Kaspi, Fernando Camilo, Science Vol. 311. no. 5769, pp. 1901 - 1904

[16] Is There a Cosmological Constant?, Kochanek, C. S., arXiv:astro-ph/9510077

[17] Small device C compiler project, `http://sdcc.sourceforge.net/`

[18] OpenCores project, `http://www.opencores.org/`

[19] Making $h(t)$ for LIGO, Xavier Siemens, Bruce Allen , Jolien Creighton , Martin Hewitson, Michael Landry, 2004 Class. Quantum Grav. 21 S1723-S1735

[20] V. Dergachev, "Description of PowerFlux Algorithms and Implementation", LIGO technical document LIGO-T050186 (2005), available in `http://admdbsrv.ligo.caltech.edu/dcc/`

[21] Unified approach to the classical statistical analysis of small signals, G. J. Feldman and R. D. Cousins, *Phys.Rev.* D **57**, 3873 (1998).

[22] LIGO: The Laser Interferometer Gravitational-Wave Observatory, B. Abbott *et al.* (The LIGO Scientic Collaboration), 2009 Rep. Prog. Phys. 72 076901

[23] Cryogenic systems of the Cryogenic Laser Interferometer Observatory Takashi Uchiyama et al 2006 J. Phys.: Conf. Ser. 32 259-264

[24] Beating the Spin-Down Limit on Gravitational Wave Emission from the Crab Pulsar, B. Abbott *et al.* (The LIGO Scientific Collaboration), 2008 ApJ 683 L45-L49

[25] Photodiode Front Ends - The REAL Story, Philip C. D. Hobbs, 42 Optics & Photonics News, April 2001

[26] The Breaking Strain of Neutron Star Crust and Gravitational Waves, C. J. Horowitz, and Kai Kadau, Phys Rev. Letters 102, 191102 (2009)

[27] Maximum Elastic Deformations of Compact Stars with Exotic Equations of State, Benjamin J. Owen, Phys. Rev. Lett. 95, 211101 (2005)

[28] The Australia Telescope National Facility Pulsar Catalogue, R. N. Manchester, G. B. Hobbs, A. Teoh and M. Hobbs, The Astronomical Journal 129 1993-2006, see also `http://www.atnf.csiro.au/research/pulsar/psrcat/`

[29] The birthrate and initial spin period of single radio pulsars, R. Narayan, Astrophys. J. 319, 162179, 1987

[30] Binary and Millisecond Pulsars, Duncan R. Lorimer, Living Rev. Relativity 11, (2008), 8. URL (cited on 2009-08-15): http://www.livingreviews.org/lrr-2008-8

[31] Neutron Star Population Dynamics. II. Three-dimensional Space Velocities of Young Pulsars, J. M. Cordes and D. F. Chernoff, Astrophys. J. 505, 315 (1998)

ABSTRACT

AN ALL-SKY SEARCH FOR CONTINUOUS GRAVITATIONAL WAVES

by

Vladimir Dergachev

Chair: Keith Riles

Gravitational radiation is a direct consequence of general relativity, yet to this day only indirect confirmation of its existence has been obtained.

LIGO is an experiment that aims to detect gravitational waves by comparing the lengths of the two arms of Michelson interferometers. It has recently reached design sensitivity, and a number of searches for intermittent and continuous signals are underway. In particular, isolated rotating neutron stars are expected to emit gravitational radiation of nearly constant frequency and amplitude.

Because the gravitational wave signal amplitudes are thought to be extremely weak, long time integrations must be carried out to detect a signal. The search is complicated by the motion of the Earth (daily rotation and orbital motion) which induces substantial modulations of detected frequency and amplitude that are highly dependent on source location. Large amounts of acquired data make this search computationally difficult.

We describe our search for such signals using an algorithm called PowerFlux and provide upper limits. In particular, at 153 Hz we obtain a sensitivity of 4.25×10^{-25} for circularly polarized sources in the polar sky region. At a signal frequency of 1100 Hz we are sensitive to neutron stars of ellipticity of $\sim 10^{-6}$ at distances up to 500 pc.

We also describe a prototype for a high-sampling-rate wavefront camera that can be used to monitor laser beam characteristics at radio frequencies.